REVIEW ARTICLE

Check for updates

Probing surface wetting across multiple force, length and time scales

Dan Daniel [1]✉, Maja Vuckovac[2], Matilda Backholm [2], Mika Latikka[2],
Rahul Karyappa[3], Xue Qi Koh[3], Jaakko V. I. Timonen [2],
Nikodem Tomczak [3]✉ & Robin H. A. Ras [2]✉

Surface wetting is a multiscale phenomenon where properties at the macroscale are determined by features at much smaller length scales, such as nanoscale surface topographies. Traditionally, the wetting of surfaces is quantified by the macroscopic contact angle that a liquid droplet makes, but this approach suffers from various limitations. In recent years, several techniques have been developed to address these shortcomings, ranging from direct measurements of pinning forces using cantilever-based force probes to atomic force microscopy methods. In this review, we will discuss how these new techniques allow for the probing of surface wetting properties in far greater detail. Advances in surface characterization techniques will improve our understanding of surface wetting and facilitate the design of functional surfaces and materials, including for antifogging and antifouling applications.

O ver the decades, a myriad of surfaces with unique wetting properties have been developed[1–3], including lotus-effect superhydrophobic surfaces[1,2,4], petal-effect surfaces with controllable droplet adhesion[5,6], superomniphobic surfaces that can repel both water and oil[7–9], antifouling lubricated surfaces[10–13], slippery omniphobic covalently attached liquid (SOCAL) surfaces[12,14], as well as underwater superoleophobic surfaces[15,16]. These functional surfaces have applications in many different areas ranging from anti-icing[17] to antifouling coatings[18,19] for drag reduction in ships[20,21]. The different surfaces vary widely in terms of their wetting forces, with adhesion and friction forces $F_{fric,adh} > 80$ μN for a millimetric droplet on a petal-effect surface (Fig. 1a) and $F_{fric} < 2$ μN for equivalent droplet on a lubricated surface (Fig. 1b)[10,22].

The most common method to characterize surface wettability is to measure the contact angles that a millimetric droplet makes on the surface (contact angle goniometry), and in recent years there have been several excellent review and perspective papers on the subject[23–26]. Traditionally, liquid-repellent surfaces (e.g., superhydrophobic and superoleophobic) are associated with high contact angles $\theta > 150°$ and low contact angle hysteresis $\Delta\theta < 10°$ [27,28]. However, in the last decade or so, new surface classes have been developed (e.g., SOCAL[12,14] and lubricated surfaces[10,29]) whereby droplets exhibit relatively low $\theta < 110°$ but nevertheless retain low $\Delta\theta < 5°$ and are highly mobile (See for example Fig. 1b). The interpretation of contact angle measurements is therefore more complex than commonly assumed[30–32]. This is especially true for some surface classes where the droplet is not contacting the underlying solid substrate and there is no three-phase contact line, such as lubricated surfaces and some underwater superoleophobic surfaces[33,34].

Surface wettability arises from a complex interplay between surface topography at the micro-/nano-scale and surface chemistry at the molecular scale, which is not readily captured by

[1] Division of Physical Sciences and Engineering, King Abdullah University of Science and Technology (KAUST), Thuwal 23955-6900, Saudi Arabia. [2] Department of Applied Physics, Aalto University, P.O. Box 15100, 02150 Espoo, Finland. [3] Institute of Materials Research and Engineering, A*STAR (Agency for Science, Technology and Research), 2 Fusionopolis Way, Innovis, Singapore 138634, Singapore. ✉email: danield@kaust.edu.sa; tomczakn@imre.a-star.edu.sg; robin.ras@aalto.fi
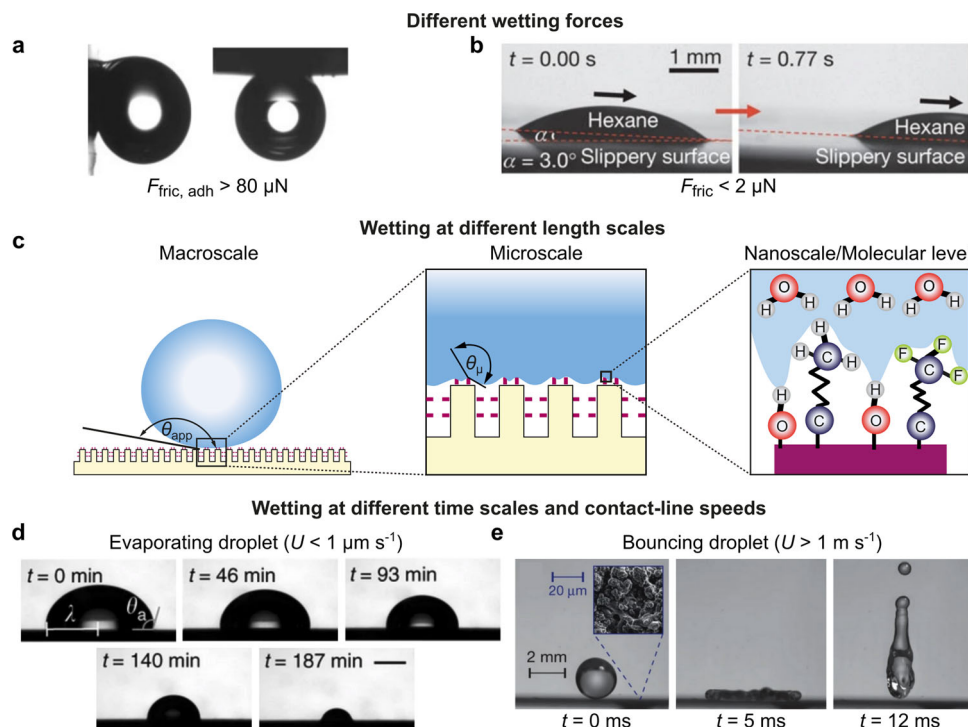
Fig. 1 Complex nature of surface wetting properties/phenomena spanning different force, length and time scales. Wetting forces can range from (**a**) more than 80 μN for a water droplet on a nanopillared surface[22] to (**b**) less than 2 μN for a hexane droplet on a slippery lubricated surface[10]. **a**, **b** Reprinted with permission from refs. [22] and [10]. **c** Wetting at the macroscale depicting a measurable apparent contact angle θ_{app} with insets highlighting the microscopic contact angle θ_μ at the contact line, and at an even smaller scale, the molecular interactions that ultimately give rise to surface wetting properties. Time scales for wetting phenomena can range from (**d**) hours for an evaporating droplet to (**e**) milliseconds for a bouncing droplet. Scale bar is 2 mm in (**d**). **d**, **e** Reprinted with permission from refs. [37] and [39], respectively.

conventional contact angle measurements (Fig. 1c). For example, the macroscopic apparent contact angle θ_{app} typically reported in contact angle measurements can be different from the microscopic contact angle θ_μ near the contact line[31,35,36]. Contact angle goniometry is typically performed for a contact line that is either not moving (static) or moving at low speeds (quasi-static), even though wetting phenomena often involve contact lines moving over a wide range of speeds. For example, a millimetric-sized droplet evaporates within a time scale of hours, and the contact line retracts at a speed of ~1 mm h^{-1} or 0.3 μm s^{-1} (Fig. 1d)[37]. In contrast, a similarly-sized water droplet bounces off a super-hydrophobic surface within ~10 ms, which translates to a contact line speed of ~m s^{-1} (Fig. 1e)[38,39].

In this review paper, we start by briefly summarizing contact angle goniometry, since it remains a useful and popular technique. We then discuss another popular method, Wilhelmy plate tensiometry, which measures the wetting forces during the immersion and emersion of a surface into and from the liquid. While Wilhelmy plate tensiometry is fundamentally a force-based method, traditionally the measured forces are converted into contact angle values for easy comparison with goniometry results[40]. We then highlight new force-based methods (beginning in the 1990s) which directly measure wetting forces, in particular $F_{fric,adh}$, for a droplet/colloid interacting with the surface (Box 1). The droplet/colloid probe can be millimetric for force probe methods[29,35,41–43] or micron-sized for atomic force microscopy methods[44,45]. Finally, we briefly outline other less commonly used techniques, such as the oscillating droplet tribometer[46] and centrifugal adhesion balance[47,48]. These two techniques, while less versatile, have the ability to generate larger forces and simulate the effects of higher gravitational pull.

In this paper, we also highlight the difference between static/quasi-static and dynamic measurements. For example, contact angle goniometry is primarily a static/quasi-static measurement that quantifies the properties of a stationary or slowly moving contact line, whereas Wilhelmy plate tensiometry and the newer force-based methods can perform dynamic measurements for contact lines moving at controlled speeds. The distinction between static/quasi-static and dynamic measurements is often neglected in the literature despite the fact that wetting forces can be very different for the two cases[49,50]. The measurement techniques described here have their strengths and weaknesses, but they complement one another and when combined allow us to probe surface-wetting properties across multiple force, length, and time scales in unprecedented detail.

Contact angle goniometry

Since Thomas Young first defined contact angle in his seminal 1805 paper[51], it has become the most commonly accepted measure of surface wettability. The contact angle is an easily understood concept since it allows us to relate the macroscopic droplet shape to the surface wetting properties. The most common method to measure contact angles is by using contact angle goniometry (Fig. 2)[23–26,52–54] which is easy to implement since it only requires good lighting and a high-resolution camera. To measure the static apparent contact angles θ_{stat}, a millimetric-sized droplet is placed carefully on the sample, its profile is then imaged by a camera, and the contact angles are determined by fitting the droplet's profile with a suitable physical model, e.g., Young-Laplace equation (Fig. 2a)[36,52]. θ_{stat} provides valuable information about surface wetting properties but lacks information about the wetting origin and droplet mobility over the

Box 1 | Development of surface wetting characterization techniques

Traditionally, surface wetting is quantified by either contact angle goniometry or Wilhelmy plate tensiometry, which both measure contact angles. Both techniques have remained popular and useful for over a century[51,67,126–128]. Beginning in the 1990s, new techniques were developed which directly measure wetting forces $F_{adh, fric}$ rather than rely on contact angle measurements, a conceptual break from previous techniques. Dimensions indicated for the atomic force microscopy methods refer to either the tip or droplet/colloid radius.
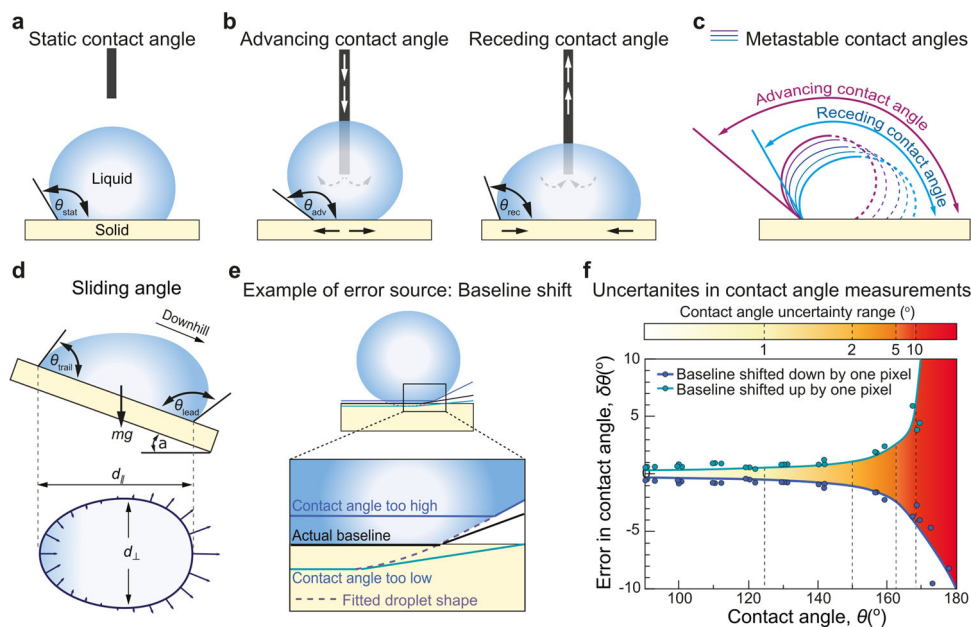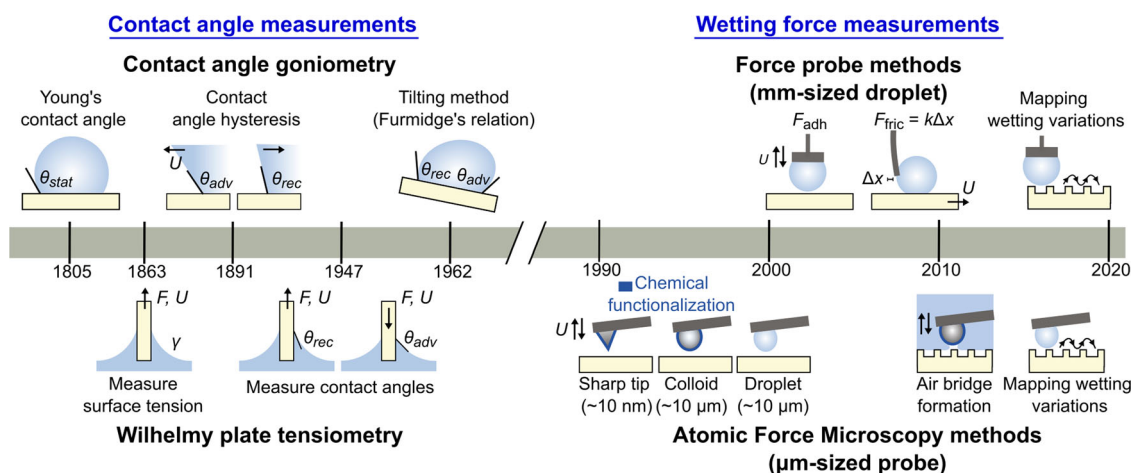
Fig. 2 Contact and sliding angle measurements. Schematic illustrations for (**a**) a sessile droplet forming an apparent static contact angle θ_{stat} on a solid surface, (**b**) a volume change method to measure the advancing and receding contact angles θ_{adv} and θ_{rec}, respectively, (**c**) possible metastable contact angles on real surfaces, (**d**) the tilting plate method to determine the critical sliding angle α, (**e**) the error in contact angle measurements $\delta\theta$ arising from the misplacement of the baseline or baseline shift, and (**f**) $\delta\theta$ resulting from baseline shifts (up or down) by 1 pixel as a function of θ (modified from ref. [53]).

surfaces. For example, both lotus-leaf[1,4,55] and rose-petal surfaces[5,22] have high θ_{stat}, but very different droplet mobilities. Droplet rolls off easily on a lotus leaf[1,4,55] while it stays pinned on a rose petal even after the petal is entirely inverted[22]. Thus, θ_{stat} does not fully describe the surface wetting properties[52].

To quantify droplet mobility, we can measure the advancing and receding contact angles θ_{adv} and θ_{rec}, respectively. This is achieved by slowly and quasi-statically increasing and decreasing the droplet volume until the contact line starts to advance and recede, respectively (Fig. 2b)[52,53]. The difference between advancing and receding contact angles is defined as the contact angle hysteresis $\Delta\theta = \theta_{adv} - \theta_{rec}$[35,36,52,53] which reflects the strength of contact line pinning due to surface roughness and chemical heterogeneities; the smaller the $\Delta\theta$ value, the weaker is the pinning strength and the higher is the droplet mobility.

Contrary to an ideal solid surface that is perfectly smooth, chemically homogeneous, and characterized by a unique equilibrium contact angle[35,36], real surfaces are rough, chemically heterogeneous, and have a broad range of θ values between θ_{adv} and θ_{rec} (Fig. 2c); each θ value corresponds to one of the many possible metastable equilibrium states, and the experimentally observed θ depends on how the droplet is placed on the surface. It

is therefore insufficient to report only one value of contact angle (such as the static θ_{stat}) as a wetting parameter. Reporting $\Delta\theta$ value is more meaningful as it provides information on the range of possible metastable states and the energy barriers between them; an even better measure for surface wettability and droplet mobility is the cosine form of contact angle hysteresis or $\Delta\cos\theta = \cos\theta_{rec} - \cos\theta_{adv}$, which is directly related to the Young-Dupré work of adhesion[56] and to the lateral friction force (per unit length) required to remove a droplet (see later discussions in Eqs. (6)–(8)). However, despite recent progress[57–61], there is no complete theoretical model that relates θ and $\Delta\theta$ (or $\Delta\cos\theta$) to the surface physical properties, such as topology and chemistry.

The droplet mobility can also be quantified using the tilting plate method[35,53,62]. This is done by carefully placing a droplet on a level sample and gradually tilting the sample up to a critical tilt angle α at which the droplet starts to move. Similar to $\Delta\theta$, α quantifies the pinning strength at the contact line and hence droplet mobility: the lower the α value, the higher the droplet mobility. As we tilt the surface, the droplet deforms (Fig. 2d), and the friction force F_{fric} arising from pinning at the contact line is related to the hysteresis between the contact angles θ_{lead} and θ_{trail} at the leading and trailing edge, respectively, as $F_{fric} = \gamma K d(\cos\theta_{trail} - \cos\theta_{lead})$, where γ is the surface tension of the droplet, d is the diameter of the contact area, and K is a dimensionless factor that accounts for the precise shape of the contact line. When the droplet starts to move, F_{fric} equals the lateral component of gravity force $V\rho g \sin\alpha$, and α can be expressed as[62]

$$\sin\alpha = \frac{\gamma K d}{V\rho g}(\cos\theta_{trail} - \cos\theta_{lead}), \qquad (1)$$

where V and ρ are the droplet's volume and density, respectively, and g is the gravitational acceleration. Usually, the contact line is assumed to be circular for highly repellent surfaces, but it can be elongated along the sliding direction if there are strong pinning sites, with length $d_\parallel$ along the sliding direction larger than $d_\perp$ perpendicular to the sliding direction (Fig. 2d). To measure both $d_\parallel$ and $d_\perp$, we require either one top-/bottom-view camera or two sideview cameras perpendicular to each other; in most commercial contact angle goniometry setups, only one sideview camera is available to measure $d_\parallel$ but not $d_\perp$.

Note that $\theta_{lead} = \theta_{adv}$ and $\theta_{trail} = \theta_{rec}$ only when the leading and trailing contact lines, respectively, start to move, which can happen at different time points. In comparison, the tilting angle is determined at a single time point just before the entire droplet starts to move[52,62]; therefore, at the critical α value, θ_{lead} and θ_{trail} in Equation (1) are not necessarily the same as θ_{adv} and θ_{rec}. α is an extensive quantity that depends on the droplet volume (Eq. (1)), which must be reported for reproducibility[35]. Also, α depends on the measurement protocol (e.g., how the droplet is placed on the sample, whether the needle is inside or outside the droplet during tilting, and the tilting rate), which affects the quasi-static deformation of the droplet before the onset motion. Experimentally, several groups have shown that the equalities ($\theta_{lead} = \theta_{adv}$ and $\theta_{trail} = \theta_{rec}$) are only obeyed for surfaces with low contact angle hysteresis[62,63].

So far, we have described contact angle measurements performed under quasi-static conditions for optimal reproducibility; flow rates should be low and the tilt rate should be gradual to avoid dynamic effects, such as viscous dissipation[36,52]. It is possible to measure contact angles under dynamic conditions, for example, by measuring the contact angles for contact lines moving at different speeds U[64]. However, for conventional contact angle goniometry, there is poor control of U and other more suitable methods exist to probe surface wetting properties under

dynamic conditions (e.g., Wilhelmy plate tensiometry, cantilever-based force probes, and atomic force microscopy methods, which we will discuss in later sections). The distinction between contact angles (and surface wetting properties) measured under quasi-static and dynamic conditions is either ignored or not well understood, which accounts for much of the confusion found in the literature.

Contact angle goniometry remains the most popular method to quantify surface-wetting properties because it is easy to perform and can be used for quick quality control, e.g., to observe the difference in surface-wetting properties before and after surface treatment. This method is also versatile and can be used for various surfaces (from biological to artificial samples, including metals, ceramics, polymers, minerals, plastics, and textiles) and liquids (including water, hexadecane, and even liquid metals[65]). However, contact angle measurements are less useful in probing the physical origin of the observed surface-wetting properties; surfaces with very different physical basis for their liquid-repellent properties (e.g., superhydrophobic and lubricated surfaces) can exhibit similar contact angle hysteresis values. Moreover, contact angle measurements suffer from several practical limitations. The accuracy of contact angle measurements depends on how well we can image the droplet profile and position the baseline accurately. For surfaces with very low $\theta < 40°$[66] and very high $\theta > 150°$[53,54], even a one-pixel displacement error in the baseline position can translate to error in $\delta\theta$ of more than 10° (Fig. 2e, f). For super-repellent surfaces with $\Delta\theta$ of a few degrees, this is equivalent to 300% error in contact angle hysteresis and adhesion and friction forces[53]. The θ value obtained also depends on the choice of image analysis software and the profile-fitting algorithm used (e.g., spherical cap approximation, polynomial, tangent line, and Young-Laplace fitting). There is also an element of subjectivity in contact angle measurements since the position of the baseline has to be placed manually if the automatic baseline detection algorithm fails (which happens often for surfaces with very high $\theta > 150°$). In consequence, the results obtained by independent experienced operators can easily vary up to 12° for the exactly same image[35,54].

For macroscopically rough and uneven samples, such as plant leaves, insect wings, and woven textiles, the positioning of the baseline and hence accurate contact angle measurements are even more challenging[53]. Contact angle measurements are also sensitive to external vibrations since any additional disturbances, such as airflow or surrounding room vibrations cause measurement errors[52]. Contact angle goniometry is also not suitable for small droplets (<3μL), because the presence of a needle can significantly distort the droplet profile during contact angle hysteresis measurements (Fig. 2b) and the weight of a small droplet cannot overcome the pinning force during tilting angle measurements (Fig. 2d) even when the surface is vertically inclined. Readers can follow, for example, the protocol established by Huhtamäki et al. (2018)[52] to obtain contact angle measurements with minimal errors. Finally, the method has limited spatial resolution to map wetting variations over the surface[42].

Wilhelmy plate tensiometry and capillary rise method

Wilhelmy plate tensiometry was initially developed to measure the surface tension of liquids[40,67,68], but was later adapted to determine contact angles on a surface. In this method, the test surface (typically mounted on a rectangular thin plate) is attached to a sensitive microbalance that measures changes in forces during immersion and emersion from the liquid (of known surface tension γ) with controlled speed U, and immersion depth h (Fig. 3a). The measured force F is associated with the capillary
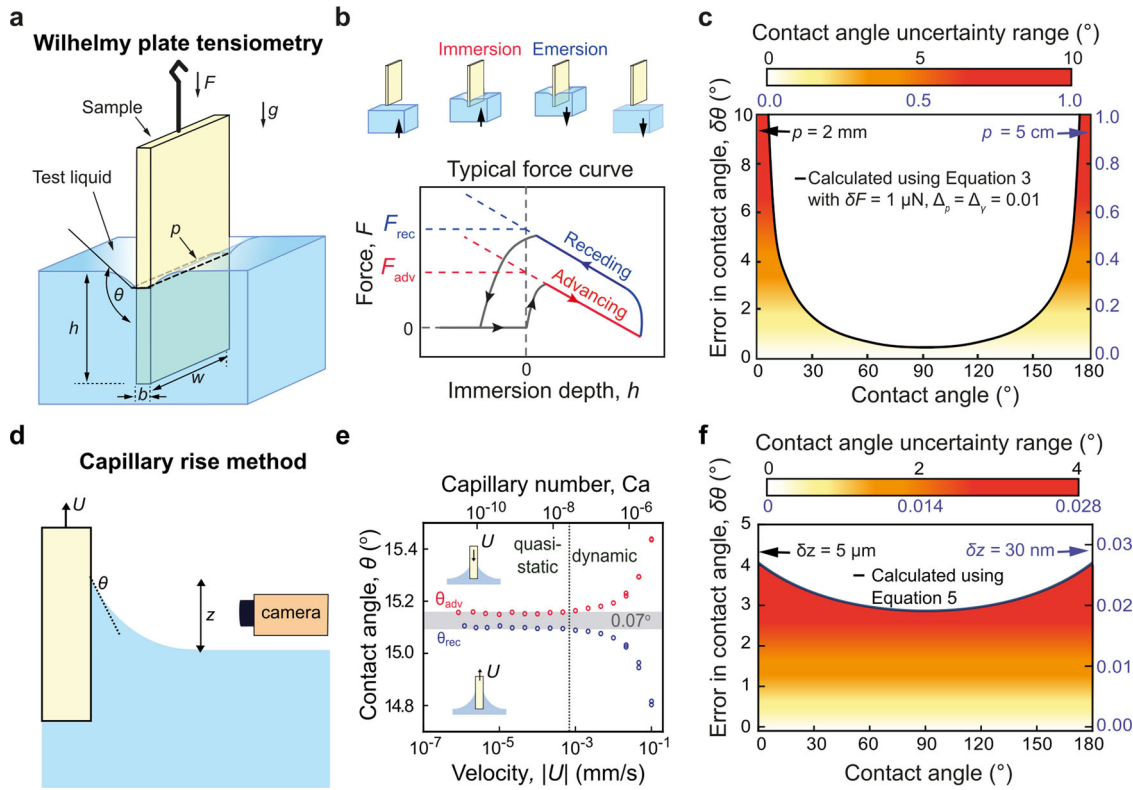
Fig. 3 Wilhelmy plate tensiometry and capillary rise method for contact angle evaluation. a Schematic illustration of the experimental setup. **b** Typical procedure to determine θ_{adv} and θ_{rec} from advancing and receding force curves F_{adv} and F_{rec} during immersion and emersion, respectively. **c** Uncertainties in θ estimates calculated with standard error propagation (Equation (3)) for two different wetted perimeters $p = 2$ mm and $p = 5$ cm (left and right y-axes, respectively). Here, we assume $\delta F = 1 \mu N$, and the relative uncertainties for the wetted perimeter $\Delta_p = \delta p/p = 0.01$ and surface tension $\Delta_\gamma = \delta \gamma/\gamma = 0.01$[75]. **d** Using the capillary rise at a vertical plate, θ can be deduced from the meniscus height z observed optically (See Equation (4)). No force measurement is required. **e** Contact angle measurements as a function of immersion (advancing) and emersion (receding) speed U. The liquid used is decane which wets the silicon surface grafted with silicone polymer brushes. Adapted from ref. [78]. **f** Error in contact angle obtained using the capillary rise method for $\delta z = 5 \mu m$ and 30 nm (left and right y-axis, respectively) and assuming that $L_c = 2$ mm (true for most liquids), as predicted by Equation (5).

force from the meniscus $p\gamma \cos\theta$ and the buoyancy force $\rho g Ah$, that is[40,68–74]:

$$F = p\gamma \cos\theta - \rho g Ah, \qquad (2)$$

where $p = 2(b + w)$ is the wetted perimeter (with b and w being the sample thickness and width, respectively), $A = w \times b$ is the cross-sectional area of the sample, ρ is the liquid density, and g is the gravitational acceleration. The recorded force versus the immersion depth curve is represented schematically in Fig. 3b[68]. $F = 0$ until the surface contacts the liquid, and the immersion and emersion are indicated by the advancing and receding curves, respectively. We can obtain θ_{adv} and θ_{rec} by extrapolating (using linear regression) the advancing and receding force curves to the zero-depth immersion ($h = 0$, no buoyancy force), i.e., $F_{adv} = p\gamma \cos\theta_{adv}$ and $F_{rec} = p\gamma \cos\theta_{rec}$[40,60]. The contact angle hysteresis (as well as its cosine form) is also readily obtained since $\Delta \cos\theta = (F_{rec} - F_{adv})/\gamma p$. Note that while we will concentrate on the Wilhelmy plate geometry, this force tensiometry method can be applied to other geometries, such as rods and fibers.

The uncertainty in contact angle measurements $\delta\theta$ can be calculated using standard error propagation

$$\delta\theta = |\cot\theta| \sqrt{\left(\frac{\delta F}{p\gamma \cos\theta}\right)^2 + \left(\frac{\delta p}{p}\right)^2 + \left(\frac{\delta\gamma}{\gamma}\right)^2}, \qquad (3)$$

where δF, δp, and $\delta\gamma$ are the uncertainties in the force, wetted perimeter, and surface tension values, respectively[75]. Most Wilhelmy plate tensiometers can measure forces down to a couple of

μN, though some high-end models can reduce δF to as small values as 10 nN. Figure 3c shows $\delta\theta$ calculated using Equation (3) for two different $p = 2$ mm and 5 cm (typical values for a fiber and a glass slide, respectively), assuming that $\delta F = 1 \mu N$, $\delta p/p = 0.01$, and $\delta\gamma/\gamma = 0.01$. When approaching the wetting extremes ($\theta < 10°$ and $\theta > 150°$) $\delta\theta$ diverges similarly as in contact angle goniometry (c.f. Fig. 2f). For $p = 2$ mm, $\delta\theta$ in the two methods, Wilhelmy plate tensiometry and contact angle goniometry, have similar values (e.g, about 10° for $\theta < 5°$ and $\theta > 175°$). However, for larger $p = 5$ cm, Wilhelmy plate tensiometry is considerably more precise than contact angle goniometry.

A closely related method is using the capillary rise at a vertical plate[76,77]. Similarly to the Wilhelmy plate tensiometry, the surface of interest is immersed into and emersed from the liquid bath. However, rather than determining θ from force measurements, we can deduce θ from the meniscus height z since

$$z = \sqrt{2(1 - \sin\theta)} L_c, \qquad (4)$$

where $L_c = \sqrt{\gamma/\rho g}$ is the capillary length (Fig. 3d). Note that the schematic in Fig. 3d depicts the case for $\theta < 90°$ and $z > 0$; for $\theta > 90°$, $z < 0$ and the meniscus position will be below the water bath.

One major strength in both Wilhelmy plate tensiometry and capillary rise method (but not in contact angle goniometry) is the good control of immersion/emersion speed U and hence of the contact line motion. It is therefore possible to probe the wetting properties of surfaces both quasi-statically (in the limit of low U) and dynamically (by varying U). Using the capillary rise
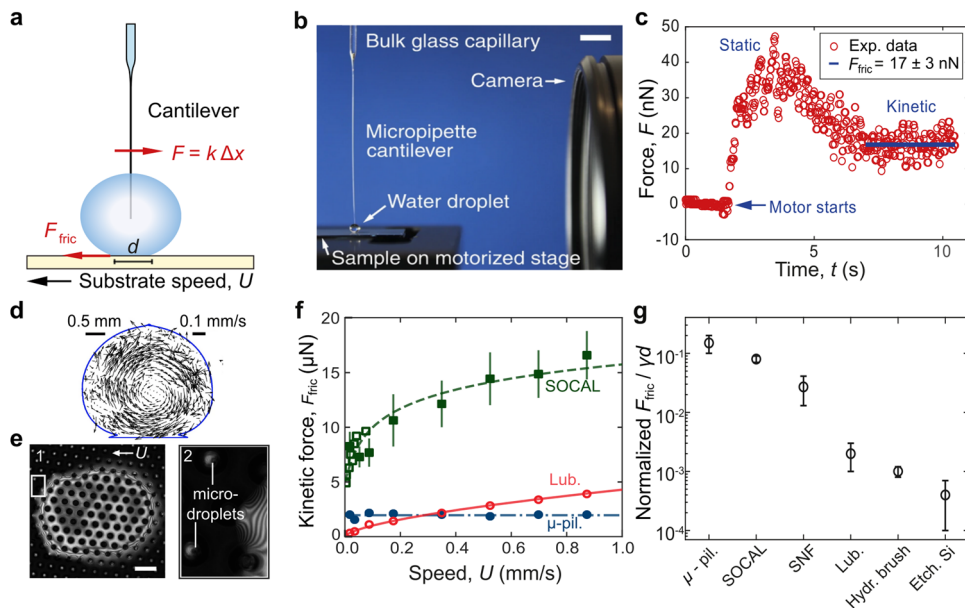
Fig. 4 Friction measurements with a cantilever-based force probe. a Schematic (not-to-scale) showing a droplet attached by capillarity to an elastic cantilever with spring constant k. The friction force acting on the droplet can be measured by moving the substrate and detecting the cantilever deflection Δx with a camera, since $F = k\Delta x$. **b** Photograph of the cantilever-based force probe. Scale bar is 5 mm. **c** Experimental force data of a water droplet moving on an extremely slippery superhydrophobic etched silicon sample, showing the initial static bump and the subsequent kinetic friction F_{fric} plateau. **d** Particle image velocimetry can be incorporated to quantify the flow profile inside the droplet[81]. **b**–**d** are reprinted with permission from ref. [81]. **e** Reflection interference contrast microscopy can be used to visualize details of droplet contact, such as contact line pinning on micropillared surface[32]. Scale bar is 0.1 mm. **f** Plot showing F_{fric} as a function of substrate speed U for different liquid-repellent surfaces. Reprinted with permission from ref. [32]. Error bars are standard deviations for three or more repeats. **g** The dimensionless friction force of drops as measured with cantilever-based techniques for different liquid-repellent samples. Reprinted with permission from ref. [81]. Error bars are for different samples and experimental conditions (e.g., droplet speeds).

approach, Lhermerout *et al.* (2016) measured θ_{adv} and θ_{rec} of decane on silicon surface grafted with silicone polymer brushes (similar to SOCAL surface in Fig. 4) by varying $|U|$ between 1 nm s^{-1} and 1 cm s^{-1} (Fig. 3e)[78]. They found that $\Delta\theta$ approaches a constant of 0.07° in the limit of $U < 1$ μm s^{-1} (quasi-static condition) but increases dynamically with increasing $U > 1$ μm s^{-1}.

Using error propagation, we can deduce the corresponding uncertainty in contact angle measurement

$$\delta\theta = \sqrt{\frac{2(1 - \sin\theta)}{\cos^2\theta}}\left(\frac{\delta z}{L_c}\right). \tag{5}$$

Here, we assume L_c is known with high precision, which is true for common liquids, such as water and alkanes. Unlike in Wilhelmy plate tensiometry, $\delta\theta$ in the capillary rise approach does not diverge in the wetting extremes ($\theta < 10°$ and $\theta > 150°$) and is instead bounded, since $\sqrt{2(1 - \sin\theta)/\cos^2\theta} \in [1, \sqrt{2}]$ (Fig. 3f). With a typical high-resolution camera, the position of the meniscus can be determined with $\delta z = 5$ μm and we expect $\delta\theta$ to be between 3° and 4° (left y-axis in Fig. 3f). Lhermerout et al. (2016) reported that they were able to minimize $\delta z = 30$ nm (by using a combination of several high-resolution cameras and image processing techniques[79]) and hence achieve a θ resolution of less than 0.03° (right y-axis in Fig. 3f)[78,79]. Despite the excellent contact angle resolution that can be achieved, the capillary rise approach is not as popular (or accessible) as Wilhelmy plate tensiometry or contact angle goniometry, partly because no commercial system is available.

Wilhelmy plate tensiometry can be used to detect surface heterogeneity with a spatial resolution of at least 250 μm, which can likely be improved with further optimization[72]. There are however limitations on the samples types that can be probed with the

Wilhelmy plate tensiometry and the capillary rise method: the samples are typically restricted to simple geometries with a uniform cross-section (such as plates, fibers, and rods) so that the wetted perimeter p is constant during the wetting process[74]. For irregularly shaped samples, an additional image processing step has been proposed to calculate the effective sample perimeter and volume as a function of the immersion depth[80], but this can be difficult to implement and can induce more errors in the contact angle estimates.

Another requirement is the need for the sample to be perfectly vertically aligned, as any slight tilt can lead to uncertainties in force readout and meniscus height and, consequently, contact angle estimates[40]. For Wilhelmy force measurements, there are additional requirements, such as the need for samples to be flat and homogeneous on at least one but optimally two sides[40,72]. The samples should also have a uniform cross-section so that the wetted perimeter p is constant during the wetting process. Such requirements are often not met in biological samples, such as insect wings or plant leaves, which are naturally curved and uneven. Some biological samples can also be too fragile to be secured onto the Wilhelmy plate.

The Wilhelmy plate and capillary rise methods are sensitive to temperature change and disturbance caused by airflow, and thus the experimental chamber needs to be completely sealed[40]. The methods also lack spatial resolution since they are based on the immersion process and thus are not optimal for measuring the spatial wetting variations at different locations on the surface. Finally, the time resolution of the methods (usually 50 Hz) is not suitable for the detection of fast dynamical processes that occur in wetting.

Wetting force measurements
The techniques described in the previous sections—goniometry, Wilhelmy plate tensiometry, and capillary rise method—are all

Table 1 Elastic cantilevers that have been used to measure drop friction on various substrates.

Cantilever type	Length (cm)	Width (μm)	k (nN/μm)	Resolution (nN)
Rectangular glass capillaries[41,49]	3.5 − 5	40 − 400	100 − 200	~40
Polymeric tubes[29,32,33]	6 − 10	360	2 − 30	10 − 100
Glass micropipettes[81,86]	1.5 − 3	~30	0.1 − 200	~1

contact angle based methods, with goniometry primarily a quasi-static method, while the other two techniques can perform both quasi-static and dynamic measurements.

Starting in the 1990s, new techniques were developed to measure wetting forces on surfaces directly rather than relying on contact angle measurements. Using closely related methods, different research groups independently measured friction and adhesion forces $F_{fric,adh}$ for droplets interacting with various surfaces (superhydrophobic[41,81,82], lubricated[29], and underwater superoleophobic[33]). The droplet can be millimetric in size in the case of force probe methods[29,33,41,81,82] or tens of micrometers for atomic force microscopy (AFM) methods[45,83–85]. Traditionally, liquid-repellent surfaces with low contact angle hysteresis $\Delta\theta$, such as superhydrophobic and superoleophobic surfaces, are associated with both low adhesion and low friction; however, some of the newer surface classes (e.g., lubricated surfaces and SOCAL) exhibit ultra-low friction but high adhesion. It is therefore important to report not just $\Delta\theta$ or F_{fric} but also F_{adh} to fully describe the repellent properties of a surface.

For most surfaces where the contact angles θ are well defined, the wetting forces can be related to θ. For example, when normalized by the droplet contact diameter d and surface tension γ, the friction force (per unit length) is equivalent to contact angle hysteresis, i.e., $F_{fric}/\gamma d \sim \Delta\cos\theta$. Similarly, the normalized $F_{adh}/\gamma d$ is a function of $\sin\theta_r$, though no analytic relation exists to relate the two quantities (See later discussion and Equations (6)–(9)).

As will be discussed throughout the next sections, the force-based methods have several advantages over contact angle methods. They are generally more sensitive and can measure smaller $\Delta\theta$. Force-based methods can straightforwardly perform dynamic measurements with controlled contact-line speeds and spatially map surface wetting properties. Importantly, for some of the newer surfaces (e.g., lubricated and underwater superoleophobic surfaces) where contact angle measurements are difficult to perform and interpret, F_{fric} and F_{adh} can be measured and interpreted easily.

Force probe method (mm-sized droplet)

Lateral friction force measurements. Cantilever-based force probes are being increasingly adopted to measure the friction force (also referred to as the lateral adhesion force) of droplets moving on different surfaces (Fig. 4a)[29,32,33,41,43,49,81,82,86–89]. There are several variations of the cantilever-based technique (e.g., drop adhesion force instrument[41], capillary force sensor[88], micropipette force sensor[81], and droplet force apparatus[29,33]) but these different approaches all work under the same physical principle—a droplet is attached to the end of a cantilever with a known spring constant k, and the force F is obtained by measuring the cantilever deflection Δx using a high-resolution camera mounted from the side or using a laser deflection system[41], giving $F = k\Delta x$[90]. More recently, by raster-scanning a liquid drop over a surface and measuring the friction force, Hinduja *et al.* (2022) was able to obtain 2D characterization and imaging of surface wetting properties[82].

Various cantilevers of different materials, dimensions, and spring constants have been reported in the literature, as summarized in Table 1. Figure 4b shows a glass micropipette

cantilever that can measure forces as small as a few nanonewtons[81]. In a typical friction experiment, a drop is placed on the surface of interest and attached to the end of a slender, vertically mounted cantilever through capillary forces. The drop is then moved along the substrate by pulling the sample using a motorized stage. Initially, the drop moves with the surface, until the elastic force from the deflected cantilever overcomes the static friction force. The drop then starts sliding along the surface (as viewed in the reference frame of the substrate). By analyzing the cantilever deflection through image analysis, the static and kinetic F_{fric} friction force of the substrate can be directly determined (example of experimental data shown in Fig. 4c)[90]. Recently, Laroche et al. showed that static F_{fric} can vary by as much as 30% depending on how the drop is deposited, whereas kinetic F_{fric} is independent of drop history[91].

Different imaging modalities can also be incorporated into the setup, providing further insights into the origin of the surface-wetting properties. For example, particle image velocimetry (PIV) was used to track the internal fluid dynamics of drops while simultaneously measuring their friction force on a surface[81] (Fig. 4d). This allows the authors to discover the transition between rolling and sliding for droplets on superhydrophobic surfaces. Reflection interference contrast microscopy (RICM) can be used to visualize the details of the droplet's contact line motion[29,32]. The presence of an air film trapped beneath a water droplet sitting on a micropillared superhydrophobic surface results in interference fringes in Fig. 4e; e-2 shows the formation and breakup of water capillary bridges (resulting in microdroplets) on individual micropillars at the receding contact line.

Unlike contact angle goniometry, the speed of contact line motion U during friction force measurements is precisely controlled by the motorized stage. This is important because F_{fric} can vary as a function of U (Fig. 4f). For example, on lubricated surfaces where friction is dominated by viscous dissipation in the lubricant film, F_{fric} is proportional to $U^{2/3}$ [29], and $F_{fric} \to 0$ as $U \to 0$. This is unlike droplets on micropillared superhydrophobic surfaces, where friction is due to pinning on discrete micropillar posts[92], and F_{fric} is independent of U[32]. In contrast, on surfaces grafted with silicone brushes, known in the literature as slippery omniphobic covalently attached liquid (SOCAL) surfaces[93], F_{fric} increases monotonically with U, but unlike lubricated surfaces, $F_{fric} > 0$ as $U \to 0$.

The cantilever-based approach is applicable to a wide variety of liquids as well as surfaces with different wetting properties[32,41,43,49,88], from a wetting hexadecane drop with $\theta < 90°$ on a fluorinated silicon surface[49] to a highly non-wetting water drop with $\theta \approx 170°$ on an etched silicon superhydrophobic surface[81]. Figure 4g summarizes the non-dimensional friction force $F_{fric}/\gamma d$ for different classes of highly-repellent surfaces reported in the literature[81], including SOCAL[32], superhydrophobic micro-pillared (μ-pil.)[32], and lubricated (Lub.) surfaces discussed previously, as well as superhydrophobic silicone nanofilament (SNF)[49], and etched silicon (Etch. Si) surfaces[81]. F_{fric} is normalized by the droplet's base diameter d and surface tension γ to allow for comparison between drops of different volumes and liquids (e.g., oil vs. water)[32,81,88].

We can relate friction force measurements with contact angle measurements, since $F_{fric}/\gamma d$ scales with $\Delta\cos\theta = \cos\theta_{rec} -$

$\cos \theta_{\mathrm{adv}}$ (Furmidge's relation)[41,61,94,95]:

$$F_{\mathrm{fric}}/\gamma d \sim \cos \theta_{\mathrm{rec}} - \cos \theta_{\mathrm{adv}}$$
$$= -2 \sin \left(\frac{\theta_{\mathrm{adv}} + \theta_{\mathrm{rec}}}{2} \right) \sin \left(\frac{\theta_{\mathrm{rec}} - \theta_{\mathrm{adv}}}{2} \right). \quad (6)$$

For an extremely superhydrophobic surface with small $\Delta\theta = \theta_{\mathrm{adv}} - \theta_{\mathrm{rec}} \ll 1$ and $\theta_{\mathrm{adv}} = \pi$ or 180°, Equation (6) simplifies to

$$F_{\mathrm{fric}}/\gamma d \sim 2 \sin \left(\pi - \frac{\Delta\theta}{2} \right) \sin \left(\frac{\Delta\theta}{2} \right)$$
$$\approx \frac{\Delta\theta^2}{2}. \quad (7)$$

In contrast, for a water droplet on lubricated surfaces where $\theta_{\mathrm{adv}} \approx \theta_{\mathrm{rec}} \approx \pi/2$, Equation (6) simplifies to

$$F_{\mathrm{fric}}/\gamma d \sim 2 \sin \left(\frac{\pi}{2} \right) \sin \left(\frac{\Delta\theta}{2} \right)$$
$$\approx \Delta\theta. \quad (8)$$

Equations (6) to (8) allow us to compare normalized F_{fric} with contact angle hysteresis measurements $\Delta\theta$ (in radians). $F_{\mathrm{fric}}/\gamma d$ can reach as low as 10^{-3} and 10^{-4} for droplets on lubricated and etched silicon surfaces (Fig. 4g), which are equivalent to $\Delta\theta \sim 10^{-3}$ and 10^{-2} (or 0.06° and 0.8°), respectively. Such low hysteresis values are impossible to measure using contact angle goniometry as described in Figs. 2 and 3.

The temporal limit for measuring friction with a cantilever-based probe is set by the frame rate of the camera (typically less than 100 s^{-1}) or the read rate of an optical sensor in a laser deflection system (thousands of hertz or more)[41]. The cantilever width w should be small compared to the droplet size so as not to affect the droplet geometry. It is also important that F_{fric} does not exceed the capillary force holding the liquid attached to the cantilever $\sim \gamma w$; otherwise, the cantilever will detach from the drop. Given these limitations, cantilever-based force probe methods are most suitable for millimeter-sized droplets. By scanning the surface with the drop, it is possible to create 1D and 2D maps of the friction force, highlighting potential variations in the wetting properties[82].

The force limit is set by several factors, such as i) the cantilever spring constant (lower k gives a higher force sensitivity), ii) environmental vibrations (less vibrations translate to lower signal noise), and iii) optical detectability of the cantilever position (the higher the optical resolution of the camera, the higher the force resolution for the same cantilever spring constant). Using micropipettes as cantilevers, spring constants as low as $k \sim 0.1$ nN/μm can be achieved[90], but such soft cantilevers are susceptible to external vibrations and draft. Stiffer cantilevers vibrate less and force resolution (by lowering k) needs to be balanced with cantilever vibrations due to external noise (by increasing k). This is especially important when friction experiments are performed in air and not in a liquid environment as water is fifty-five times more viscous than air and effectively damps out external vibrations. The lowest friction force measured to date was 7 ± 4 nN for a millimetric water droplet moving on an extremely slippery superhydrophobic surface[81], using a micropipette cantilever with spring constant $k \approx 2$ nN/μm. Backholm et al. (2020) reported signal noise due to vibrations in the range of $\Delta x_{\mathrm{noise}} \approx 1.5$ μm and hence a force resolution of $\Delta F_{\mathrm{MFS}} \approx 3$ nN.

Vertical adhesion force measurements. Surface wetting can be assessed by measuring adhesion forces between the droplet and the substrate when they are brought together and separated (Fig. 5)[25,35,42,43,96–99]. In the simplest case, the adhesion measurements are performed using a commercial force

tensiometer[25,96] that comprises a droplet holder (probe disk[35], metal ring[96], cup[100], or thin capillary[101]) attached to a sensitive microbalance (similar to those used in Wilhelmy plate tensiometers described in previous section[25]), and a motorized stage for sample manipulation (in the z-direction). Typically, a 3-5 μL droplet probe is used[25,35,96] and the interaction forces as a function of time and surface vertical position are recorded. Force tensiometers can also be accompanied by a side camera which allows simultaneous droplet shape analysis (including the size of the droplet and its contact line) and contact angle extraction at various stages of the experiment (the attachment, spreading, retraction, and detachment events)[25,99]. The method is applicable for various samples (different geometries and sizes) as well as in other systems, including adhesion measurements with different liquids or gas bubbles[96,100,101]. Although commercial, plug-and-play versions of such a setup exist, the sensitivity of commercial force tensiometers is typically a couple of μN and not suitable for the most liquid-repellent surfaces; for example, adhesion forces as small as tens of nN have been reported for oil droplets on a hydrated polymer brush surface[33]. Moreover, force tensiometers typically have a time resolution of 1/50 s (unsuitable to track fast dynamic wetting processes) and lack the ability to map wetting variations across a sample (sample stage is moving only in the z-direction) with the required spatial resolution.

Recently, Liimatainen et al.[42] developed a scanning droplet adhesion microscope (SDAM) to quantify the wetting variations on surfaces (Fig. 5a). The working principle of SDAM is similar to that of the force tensiometer setup, but with several significant improvements. SDAM is equipped with a much more sensitive force sensor that can resolve nanonewton forces (as opposed to micronewton forces) with millisecond and sub-millisecond time resolutions, as well as a highly precise multi-axis sample stage (x-y-z as opposed to just the z-direction). The latter allows SDAM to spatially map wetting variations on surfaces with at least 10 μm resolution.

Figure 5b shows the force curve for a water droplet ($D = 1.4$ mm) during (i) approach with a controlled speed $U_{\mathrm{app}} = 5$ μm s^{-1}, (ii) contact, (iii) maximum compression force, (iv) retraction, and (v) detachment with a controlled speed $U_{\mathrm{ret}} = 10$ μm s^{-1} from a superhydrophobic surface. SDAM is able to detect a snap-in force F_{snap} as small as 5 nN at the point of contact (which cannot be measured using a typical tensiometer setup) and precisely quantify the adhesion force $F_{\mathrm{adh}} = 1.8$ μN required to remove the droplet completely (and F_{adh} can be as small as 20 nN as shown in Fig. 5h). It has been shown previously that F_{snap} and F_{adh} are correlated to θ_{adv} and θ_{rec}, respectively (Fig. 5c)[42,96]. This is not surprising since F depends on capillary force $\pi\gamma d \sin\theta$, where d is the diameter of the contact area. However, F does not just depend on θ but also on the Laplace pressure difference $\Delta P \approx 4\gamma/D$ between the inside and outside of the droplet of diameter D, more specifically

$$F = \pi\gamma d \sin\theta - (\pi d^2/4)\Delta P. \quad (9)$$

Along the force curve, d, ΔP, and θ are changing continuously and depend on the droplet geometry given by the Young-Laplace equation which can only be solved numerically (and not analytically) with suitable boundary conditions, including Eq. (9)[35,42]. There is therefore no straightforward way to relate F_{snap} and F_{adh} to θ_{adv} and θ_{rec}[35]; in contrast, there is a simple interpretation for F_{fric} with respect to the surface contact angle measurements (See Equations (6)–(8)).

The adhesion force can alternatively be obtained by measuring the deflection Δx of a cantilever-based force probe, as shown schematically in Fig. 5d (similar to how we measure F_{fric} in Fig. 4). Fig. 5e shows the force curve for an oil droplet ($D = 2.0$ mm) approaching and retracting with $U = 50$ μm s^{-1} from a
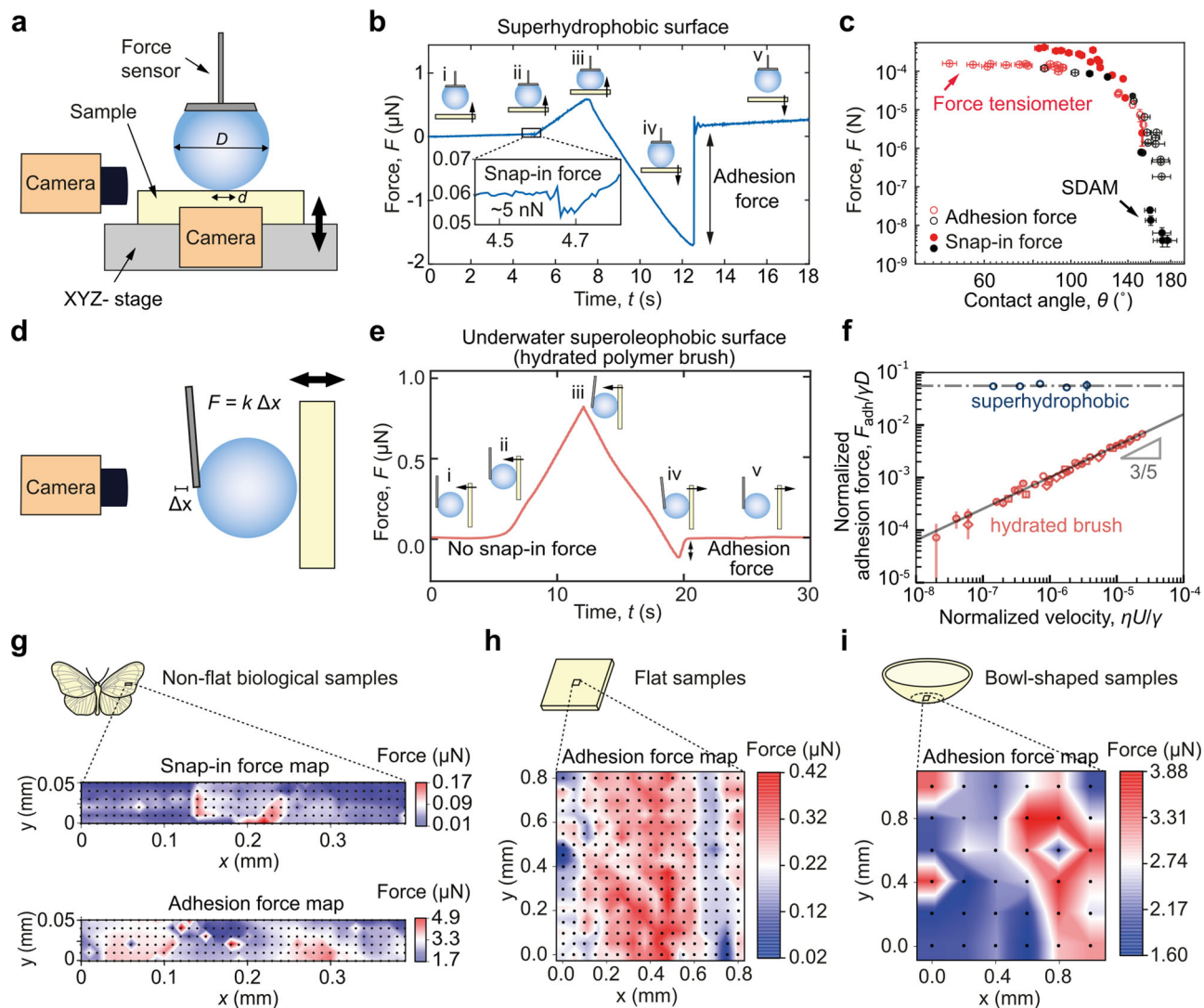
Fig. 5 Vertical adhesion force measurements. a Schematic of the scanning droplet adhesion microscope (SDAM). **b** Force curve on a superhydrophobic surface during (i) approach, (ii) contact, (iii) maximum compression force, (iv) retraction, and (v) detachment. **c** Plot showing snap-in and adhesion forces as a function of advancing and receding contact angles, respectively, for various samples measured with SDAM[42,43,97,98] and force tensiometers[96]. The error bars for contact angles are due to uncertainty in the baseline location, while the error bars for force measurements are due to sensor noise in SDAM and tensiometer. **d** Adhesion force can alternatively be measured with an elastic cantilever. **e** Force curve for an oil droplet (submerged in water) on a hydrated polymer brush surface. **f** Plot of normalized adhesion force vs. normalized velocity for oil droplets on hydrated polymer brushes (submerged in water)[33] and for water droplets on a superhydrophobic surface (in air). SDAM wetting force maps for (**g**) biological samples[42], (**h**) flat coated silicon, and (**i**) bottom of a 3D-printed bowl[98].

zwitterionic polymer brush surface underwater (adapted from ref. [33]). When submerged in water, the presence of a hydration layer prevents direct contact of the oil droplet with the underlying brushes; as a result, the surface is highly oil-repellent (super-oleophobic) and an oil droplet has a contact angle of 180° with zero contact angle hysteresis[33]. This explains why there is no observable F_{snap} and the ultra-low $F_{adh} = 85$ nN (compared with > 1 μN for similarly sized water droplet on a superhydrophobic surface).

SDAM and its cantilever-based analog are highly suited to probe dynamic wetting properties of different surfaces since the approach and retract speeds U can be controlled precisely by the motorized stage. This is important because different surfaces can have qualitatively different wetting properties depending on the speed of the contact line. Previously, we showed that F_{adh} (due to contact line pinning) is independent of U for water droplets on superhydrophobic surfaces, while F_{adh} (due to viscous forces) increases non-linearly with U ($\propto U^{3/5}$) for oil droplets on a

hydrated polymer brush surface (Fig. 5f). To compare between droplets of different sizes, we have chosen to normalize F_{adh} by γD and U by γ/η with η being the liquid viscosity. Unlike friction force measurement, it is not straightforward to normalize F_{adh} by γd because d is changing during the measurement.

By performing point-by-point measurements over a selected area (2D mapping, area scanning) and/or along the chosen line (1D mapping, line scanning) with SDAM, we can create wetting force maps (snap-in and adhesion force maps, Fig. 5g–i) to visualize wetting variations (with micron-scale resolutions) due to surface texture and chemical heterogeneity, which are generally not detectable using contact angle goniometry and commercial force tensiometers[42]. SDAM can measure a wide range of forces (between nN and mN, see Fig. 5c) and hence characterize samples with a broad range of surface wetting properties (from super-hydrophobic to hydrophilic). The size of the scanning area can range from hundreds of μm^2 to hundreds of cm^2, and the samples probed can range from flat surfaces (Fig. 5h) to non-planar

Table 2 Lateral friction and vertical adhesion forces for different surface classes. Ca = $\eta U/\gamma$ is the capillary number.

| Surface class	F_{fric}	F_{snap}	F_{adh}
Superhydrophobic	$F/\gamma d \sim \Delta \cos\theta$	$f(\theta_{adv})$	$f(\theta_{rec})$
Lubricated	$F/\gamma d \sim Ca^{2/3}$	no data	no data
Hydrated brush	$F/\gamma d \sim Ca^{2/3}$	0	$F/\gamma D \sim Ca^{3/5}$

biological samples (Fig. 5g)[42], non-transparent bowls (Fig. 5i)[98], and even slippery lubricant-infused surfaces[97]. The spatial resolution is limited by the contact area of the droplet probe. For a typical microlitre droplet, SDAM can achieve resolutions of 10 μm for superhydrophobic surfaces to a few mm for hydrophilic surfaces. The spatial resolution can potentially be improved by using smaller sub-μL droplets. This, however, should be done under special conditions, such as performing the experiment under controlled humidity or using water-glycerol droplets instead of pure water[45] to minimize pronounced evaporation of the small droplet. However, increasing the humidity and adding glycerol to water can change the surface wetting properties of the sample, resulting in different snap-in and adhesion forces[102]. Other droplet probes, including n-octane[97] and gas bubbles, can also be used with SDAM.

Comparison between friction and vertical adhesion forces. To summarize, the different variants of the force probe methods are highly suited to quantify the dynamic wetting properties of different surface classes by measuring F_{fric}, F_{snap}, and F_{adh} as a function of droplet speed U, as summarized in Table 2. The static or quasi-static wetting properties can also be quantified in the limit of $U \to 0$. Note that in friction force measurements, the speed of the contact line is equivalent to droplet speed U, whereas in adhesion force measurements, the speed of the contact line at the droplet's base (in the lateral direction) is not fixed even as the droplet speed (in the vertical direction) is fixed at U.

For superhydrophobic surfaces, the friction force is dominated by contact line pinning, and $F_{fric}/\gamma d$ scales with $\Delta \cos\theta$ and is independent of U[32,81]. Similarly F_{snap} and F_{adh} are independent of U, and are correlated to θ_{adv} and θ_{rec}, though no simple analytic function exists that relates the different quantities[42]. This is in contrast to lubricated and hydrated polymer brush surfaces where there is no contact line pinning and friction is dominated by viscous dissipation, and hence $F_{fric}/\gamma d$ scales with $Ca^{2/3}$ (where Ca $= \eta U/\gamma$ is the capillary number, and can be understood as velocity U normalized by the surface tension γ and liquid viscosity η), and unlike superhydrophobic surfaces, $F_{fric} \to 0$ as $U \to 0$ (quasi-static limit). For hydrated polymer brush surface, there is no observable F_{snap}, and $F_{adh}/\gamma D$ is equivalent to $Ca^{3/5}$. No data for F_{snap} and F_{adh} exist for lubricated surfaces, though lubricated surfaces are known to exhibit relatively high adhesion: millimetric-sized droplets remain stuck even when the surface is turned upside down[103].

Understanding the nature of F_{fric} and F_{adh} (both under dynamic conditions and in the quasi-static limit) for different surfaces can shed insights into different wetting phenomena. For example, F_{fric} (and the normalized $F_{fric}/\gamma d$) dictates contact line pinning and hence evaporation kinetics of different-sized droplets on different surfaces[104], with important applications in inkjet printing technology[105]. Similarly, F_{adh} will determine the energy loss for bouncing droplets[106], with potential applications in heat-transfer optimization[107].

Atomic force microscopy methods. Since its invention in 1986, Atomic Force Microscopy (AFM) has become a standard and
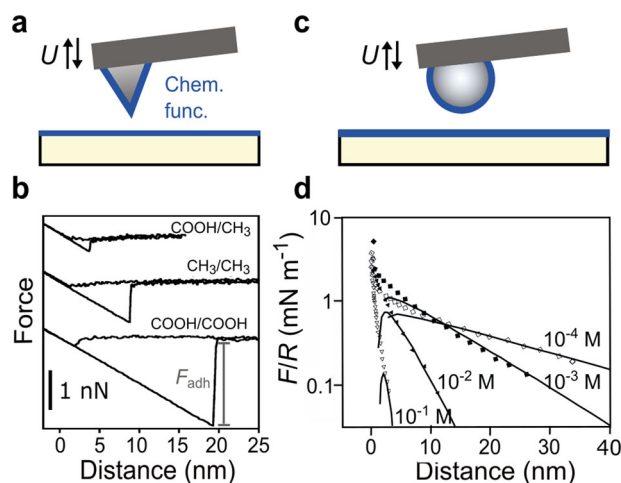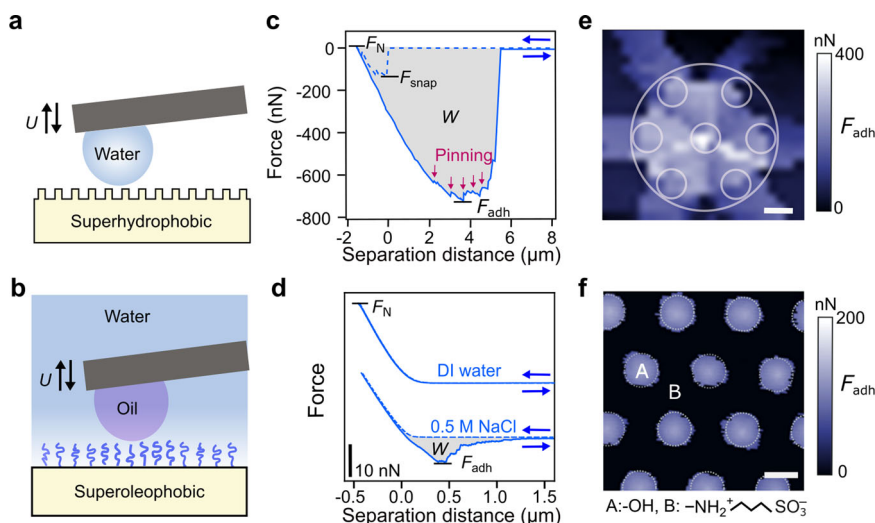

Fig. 6 Atomic Force Microscopy method. a Atomic Force Microscopy (AFM) cantilever with a sharp tip used to obtain (**b**) force spectroscopy curves for different tip/surface functionalizations. The adhesion force required to remove the tip from the surface is indicated by F_{adh}. Reprinted with permission from ref. [44]. **c** AFM cantilever with a colloidal probe used to measure (**d**) intermolecular forces that give rise to wetting properties, such as electric double-layer forces in different salt concentrations of 10^{-4}–10^{-1}M. The repulsive force F is normalized with the radius $R = 3.5$ μm of the colloidal probe. Symbols represent experimental data while solid lines are calculated from the Derjaguin-Landau-Verwey-Overbeek (DLVO) theory. Reprinted with permission from ref. [112].

powerful surface characterization tool[108]. As its name suggests, AFM is capable of measuring small forces (vertical adhesion and lateral friction forces) as a solid sharp tip interacts with the surface of interest. An AFM tip is typically made of Si or Si_3N_4, pyramidal in shape, and has a nanometric tip radius (Fig. 6a). This tip is attached to the end of a flexible cantilever, and by monitoring the displacement of the cantilever with a laser deflection system, the forces experienced by the cantilever tip can be deduced with piconewton resolution.

In chemical force microscopy, the AFM tip is modified chemically with well-defined functional groups to directly probe molecular interactions between different surface/tip chemistries (e.g., COOH/CH_3, CH_3/CH_3, and COOH/COOH). The strength of these interactions is reflected in the different magnitudes of adhesion force F_{adh} (Fig. 6b)[44,109,110]. It is also possible to spatially map chemical heterogeneities on the surface by laterally scanning the AFM tip across the surface and measuring the variations in the friction and adhesion forces. Chemical force microscopy has been, for example, used to demonstrate the heterogeneous wetting properties of natural chalk, which has important implications for oil-recovery processes[111].

It is however difficult to obtain reproducible force spectroscopy measurements using pyramidal tips or to directly compare the interactions magnitude with theoretical predictions. This is because the tip radius can vary considerably between batches (even from the same manufacturer) and the tip can get eroded after multiple measurements. To overcome this limitation, micron-sized spherical beads (i.e., colloidal probes) can be attached to the end of tipless AFM cantilevers, resulting in AFM probes with well-defined dimensions (Fig. 6c). Fig. 6d shows the repulsive electric double-layer forces F experienced by a silica glass sphere probe (radius $R = 3.5$ μm) when approaching a flat silicon surface (with 30 nm of thermal oxide) in water with different salt concentrations (10^{-4}–10^{-1}M)[112]. Here, F is normalized by the probe radius R and agrees well with predictions from Derjaguin-Landau-Verwey-Overbeek (DLVO) theory (solid

Fig. 7 Droplet Probe Atomic Force Microscopy method. By attaching (**a**) a water or (**b**) an oil microdroplet to a tipless AFM cantilever, we can characterize the wetting properties of superhydrophobic and underwater superoleophobic surfaces, respectively. **c** Typical force curve for a water droplet contacting a superhydrophobic butterfly wing. Reprinted with permission from ref. [45]. **d** The corresponding force curves for an oil droplet contacting superoleophobic hydrated brush surfaces under DI water and 0.5 M salt solution. Reprinted with permission from ref. [115]. **e** Mapping wetting variations due to topographical heterogeneities on a superhydrophobic surface. The white outline shows the micropillar structure. Scale bar is 2 μm. Reprinted with permission from ref. [45]. **f** Mapping wetting variations arising from chemical heterogeneities. Scale bar is 5 μm. Reprinted with permission from ref. [85].

lines in Fig. 6d)[113]: as the salt concentration increases and the surface charges are screened, the electric double-layer forces decrease in magnitude and decay more quickly with increasing separation distance (i.e., shorter Debye length). Electric double-layer forces have been shown to give rise to underwater superoleophobic properties of some polymer brush surfaces[33]. The ultra-sensitive force measurements and high force resolution, make AFM highly suited for probing the intermolecular forces which ultimately give rise to surface wetting properties. However, in many wetting applications, we are interested in how liquid droplets interact with the underlying surface, and the AFM techniques described above (with either a pyramidal solid tip or a colloidal probe) poorly approximate droplet-surface interactions.

Recently, several groups have attached micron-sized liquid drops to AFM cantilevers, to provide a direct method to investigate droplet-surface interactions, a technique also known as droplet probe AFM[45,84,114,115]. The working principle of droplet probe AFM is similar to the previously discussed force probe methods except for a much smaller droplet probe size and hence significantly improved spatial resolution achieved.

Droplet probe AFM has been used to investigate the wetting properties of different surfaces (Fig. 7a, b), including super-hydrophobic surfaces in air[45] and superoleophobic surfaces underwater (e.g., polyzwitterionic brush surfaces)[84,115]. While it is common to think of underwater superoleophobic surfaces as analogous to superhydrophobic surfaces in air, Daniel et al.[85] showed that the two surface classes are qualitatively different. The presence of a stable air layer in superhydrophobic surfaces minimizes but does not completely eliminate droplet contact (and hence contact line pinning). As a result, when a water droplet (diameter $D = 30$ μm) contacts a superhydrophobic surface, there is an observable snap-in force $F_{snap} = 130$ nN (Fig. 7c). Contact line pinning also results in force jumps in the retract curve (indicated by arrows in Fig. 7c), and in a significant adhesion force $F_{adh} = 720$ nN and work $W = 6$ pJ required to remove the droplet from the surface. In contrast, the presence of a hydration layer stabilized by electric double-layer forces completely eliminates contact line pinning for polyzwitterionic brush surfaces. For an oil droplet of similar size (diameter $D = 26$ μm) contacting zwitterionic poly(3-sulfopropyl methacrylate)

brush surface submerged in deionized (DI) water, there is no measurable F_{snap}, F_{adh}, or W (Fig. 7d).

The presence of dissolved salt (0.5 M NaCl) can however screen electric double-layer forces and results in measurable $F_{adh} = 6$ nN and work $W = 3$ fJ, though still significantly smaller than those observed in superhydrophobic surfaces. With droplet probe AFM, it is also possible to spatially map the wetting variations due to topographical (Fig. 7e) and chemical hetero-geneities (Fig. 7f) with micron-scale resolution.

AFM is therefore a highly versatile technique that can be used for different liquid droplet probes (e.g., water and oil) and in different ambient environments (e.g., in air and under water). It can measure very small forces (between pN to hundreds of nN) as a function of separation distance (with sub-nanometric resolution). The size of the scanned area can range from nm^2 to hundreds of μm^2. The spatial resolution depends on the size of the probe: for a pyramidal tip, the spatial resolution is in the order of nm, while for micron-sized droplet probes, the resolution is reduced to ~μm. AFM is especially suited to study fast wetting dynamics (< 1 ms), because it has excellent temporal resolution limited by the read rate of the laser deflection system (typically up to MHz).

The AFM techniques described above (especially droplet probe AFM) greatly complement the force probe method described earlier in Figs. 4 and 5. AFM has also been used to study nanoscale wetting properties either by imaging the contact line of nanodroplets[116] or by quantifying the pinning strength of individual nanometric defects[117], but this is outside the scope of this review.

Other methods

We briefly discuss two other methods which also measure wetting forces: the Oscillating Droplet Tribometer (ODT)[46,118] and the Centrifugal Adhesion Balance (CAB)[47,48]. However, unlike the force-based methods described earlier, there is poor control of contact-line speed. ODT measures F_{fric} dynamically but with a constantly changing contact line speed, whereas CAB measures both F_{fric} and F_{adh} but in a quasi-static fashion.

The ODT measures friction force from the oscillatory motion of a magnetic liquid droplet under the influence of a magnetic potential well. A small amount of superparamagnetic
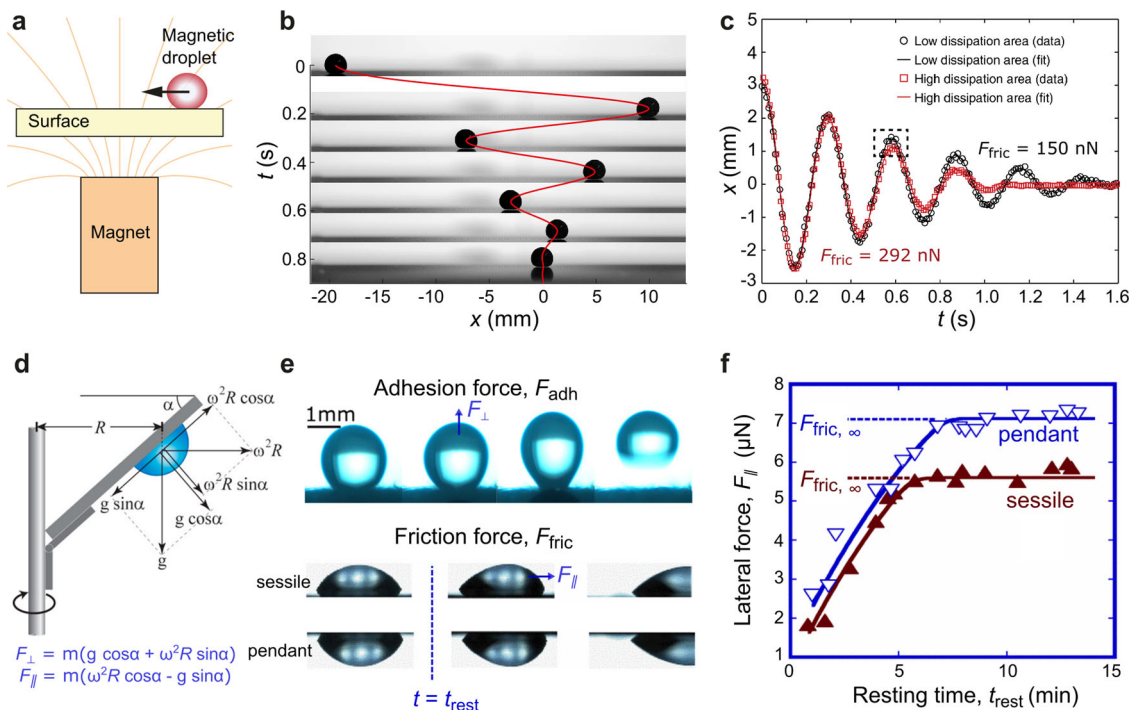
Fig. 8 Oscillating droplet tribometer and centrifugal adhesion balance. a Schematic of the oscillating droplet tribometer. **b** Snapshots of the magnetic droplet oscillating around the magnet axis (x = 0 mm). The droplet trajectory is shown in red. Reprinted with permission from ref. [118]. **c** Droplet position x as a function of time t on two different spots on the same superhydrophobic surface. The difference in the oscillation damping rates indicates variation in surface wetting properties. Reprinted with permission from ref. [46]. **d** Schematic of the centrifugal adhesion balance, which can be used to measure (**e**) the adhesion force F_{adh} and the friction force F_{fric}. Reprinted with permission from ref. [48]. **f** F_{fric} increases with the resting time of the droplet t_{rest} up to a plateau value $F_{fric,\infty}$. Reprinted with permission from ref. [47].

nanoparticles are added to the carrier liquid (e.g., water), such that the resultant droplet can be actuated using magnetic fields but without changing (or minimally changing) the liquid's other physical properties, such as its density, surface tension, and viscosity[119–123]. A permanent magnet is placed below the test surface to generate the magnetic potential well and drive the oscillatory motions.

At the beginning of the measurement, the magnetic droplet is released away from the magnet's central axis, i.e., at the edge of the magnetic potential well (Fig. 8a). The magnetic force pulls the droplet towards the magnet's central axis, inducing an oscillatory motion, which is damped by the frictional forces (Fig. 8b). The droplet motion on a superhydrophobic surface can be modeled as a damped harmonic oscillator with velocity-independent friction force F_{fric} (due to contact line pinning) and velocity-dependent viscous dissipation force (due to fluid flow inside the droplet). By measuring the damping rate of the oscillations, the friction forces F_{fric} acting on the droplet can be measured with nanonewton resolution. Figure 8c shows the oscillatory motions of a millimetric-sized magnetic droplet on two different areas of a superhydrophobic surface with two different damping rates corresponding to F_{fric} = 150 nN (colored black) and F_{fric} = 292 nN (colored red).

Figure 8d shows the schematic for the centrifugal adhesion balance (CAB) for a pendant droplet; for a sessile droplet, the test surface can be flipped. With CAB, it is possible to generate and measure forces perpendicular and parallel to the test surface $F_\perp$ and $F_\parallel$ using a combination of gravitational and centrifugal forces. Importantly, $F_\perp$ and $F_\parallel$ can be independently adjusted by changing the tilt angle α, the position of the droplet from the rotation axis R, and the rotation frequency ω. Note that R here is different from the droplet radius R in previous sections.

CAB can be used to determine the adhesion force F_{adh} by gradually increasing ω and noting the $F_\perp$ value (while maintaining $F_\parallel = 0$) required to detach the droplet from the surface (Fig. 8e). The friction force F_{fric} can be similarly determined by noting the $F_\parallel$ value (while keeping $F_\perp = 0$ or constant) required to move a droplet laterally on the surface. Tadmor et al. (2009) reported that F_{fric} is higher for a pendant droplet than for a sessile droplet, and that F_{fric} increases with the rest time t_{rest}, i.e., the amount of time the droplet was stationary before applying $F_\parallel$[47] (Fig. 8f).

There are some important similarities between the two seemingly very different techniques. Both techniques make use of body forces (magnetic forces for ODT and centrifugal forces for CAB) to actuate the droplet. The ability to generate body forces also means that the effective gravitational acceleration g_{eff} experienced by the droplet can be tuned with ODT and CAB (but not for other techniques). For ODT, bringing the magnet closer to the surface effectively simulates larger pulling force on the droplet $g_{eff} > 1 g$, where $g = 9.81$ m s^{-2} is the earth's gravitational acceleration. Depending on the centrifugal force and how the surface is positioned, CAB can effectively simulate larger pulling force $g_{eff} > 1 g$, zero-gravity situation $g_{eff} = 0$, and also a pushing force $g_{eff} < 0$ which is used to determine F_{adh}.

There are however significant differences between the two techniques. In ODT, F_{fric} is measured dynamically with fast-moving droplet with typical speeds $U \sim 0.1$ m s^{-1}, while CAB is primarily a quasi-static technique that measures static F_{fric} and F_{adh} at the point when the droplet starts to move. ODT is most suitable to quantify ultra-low $F_{fric} < 1 \mu$N for droplets on highly liquid-repellent surfaces, while CAB is more suitable for surfaces with more pinning, i.e., large $F_{fric/adh} \gtrsim mg$, where mg is the droplet's weight.

Outlook

We have described a wide range of surface wetting characterization techniques and outlined their working principles. We have

Table 3 Comparison between different surface-wetting characterization techniques.

Method	Type	Droplet size	F range	U range	Spatial resolution	Time resolution
Goniometry	static/quasi-static	~ mm	$10^{-5} - 10^{-4}$ N	$10^{-6} - 10^{-4}$ m s^{-1}	~ mm	10^{-2} s
Wilhelmy	dynamic	–	$10^{-8} - 1$ N	$10^{-9} - 10^{-1}$ m s^{-1}	250 μm	10^{-2} s
Force probe	dynamic	0.1 – 5 mm	$10^{-9} - 10^{-3}$ N	$10^{-9} - 10^{-1}$ m s^{-1}	10 μm	10^{-3} s
AFM	dynamic	1 – 100 μm	$10^{-12} - 10^{-5}$ N	$10^{-10} - 10^{-2}$ m s^{-1}	1 μm	10^{-6} s
ODT	dynamic	~ mm	$10^{-8} - 10^{-6}$ N	$10^{-2} - 10^{-1}$ m s^{-1}	~ cm	10^{-3} s
CAB	static/quasi-static	~ mm	$10^{-6} - 10^{-4}$ N	–	~ mm	10^{-2} s

also made the important distinction between static/quasi-static and dynamic measurements. The techniques described in this review have their own strengths and limitations, as summarized in Table 3. For example, force probe methods are more suited for larger millimetric-sized droplets (resulting in a spatial resolution of 10 μm), while AFM methods can only be used in combination with smaller, micron-sized droplets (resulting in a spatial resolution of 1 μm). Measurement techniques such as force probe, AFM, and ODT can access lower force ranges and are best suited to characterize highly-repellent surfaces, while CAB which can generate larger body forces is best implemented for highly-pinning surfaces. To achieve the best performance (especially in terms of spatial resolution and F range), it is important to perform the experiments in a vibration-free environment (e.g., inside an environmental chamber and on top of an optical table). In most experimental setups there is often poor or no control over temperature and humidity levels—important factors to improve on in future work, especially when there are surface electrostatic charges present which can greatly impact surface properties[124,125].

The different techniques described here can complement one another, and when considered together, offer an unprecedented range of accessible experimental parameters, i.e., the values for the droplet probe size, and magnitudes in F and U. A better appreciation of the techniques' strengths and weaknesses will also allow the reader to best choose the best characterization technique for their wetting application, e.g., measuring quasi-static wetting properties for an evaporating droplet or dynamic wetting properties for a bouncing droplet. We envision the combination of the various techniques will be especially useful when studying surface wetting by complex, non-newtonian fluids (e.g., ketchup, printer ink, and various colloidal suspensions; all of which have important industrial applications), whose rheological and hence wetting properties can vary over orders of magnitude with shear rate, applied stress, and time.

Data availability

References

1. Bhushan, B. & Jung, Y. C. Natural and biomimetic artificial surfaces for superhydrophobicity, self-cleaning, low adhesion, and drag reduction. *Prog. Mater. Sci.* **56**, 1–108 (2011).
2. Nishimoto, S. & Bhushan, B. Bioinspired self-cleaning surfaces with superhydrophobicity, superoleophobicity, and superhydrophilicity. *RSC Adv.* **3**, 671–690 (2013).
3. Zhang, X., Shi, F., Niu, J., Jiang, Y. & Wang, Z. Superhydrophobic surfaces: from structural control to functional application. *J. Mater. Chem.* **18**, 621–633 (2008).
4. Barthlott, W. & Neinhuis, C. Purity of the sacred lotus, or escape from contamination in biological surfaces. *Planta* **202**, 1–8 (1997).
5. Zhu, H., Guo, Z. & Liu, W. Adhesion behaviors on superhydrophobic surfaces. *Chem. Commun.* **50**, 3900–3913 (2014).
6. Liu, Z. et al. Temperature-based adhesion tuning and superwettability switching on superhydrophobic aluminum surface for droplet manipulations. *Surf. Coat.* **375**, 527–533 (2019a).
7. Tuteja, A. et al. Designing superoleophobic surfaces. *Science* **318**, 1618–1622 (2007).
8. Tuteja, A., Choi, W., Mabry, J. M., McKinley, G. H. & Cohen, R. E. Robust omniphobic surfaces. *Proc. Natl Acad. Sci. USA* **105**, 18200–18205 (2008).
9. Li, J. et al. Oil droplet self-transportation on oleophobic surfaces. *Sci. Adv.* **2**, e1600148 (2016).
10. Wong, T.-S. et al. Bioinspired self-repairing slippery surfaces with pressure-stable omniphobicity. *Nature* **477**, 443–447 (2011). **Early paper on lubricated surfaces which sometimes do not have three-phase contact lines**.
11. Lafuma, A. & Quéré, D. Slippery pre-suffused surfaces. *Europhys. Lett.* **96**, 56001 (2011). **Another early paper on lubricated surfaces**.
12. Barrio-Zhang, H. et al. Contact-angle hysteresis and contact-line friction on slippery liquid-like surfaces, *Langmuir*, 15094–15101 (2020).
13. Armstrong, S., McHale, G., Ledesma-Aguilar, R. & Wells, G. G. Evaporation and electrowetting of sessile droplets on slippery liquid-like surfaces and slippery liquid-infused porous surfaces (SLIPS). *Langmuir* **36**, 11332–11340 (2020).
14. Wang, L. & McCarthy, T. J. Covalently attached liquids: Instant omniphobic surfaces with unprecedented repellency. *Angew. Chem. Int. Ed.* **55**, 244–248 (2016). **Early paper on SOCAL surface which has relatively low contact angle but ultra-low contact angle hysteresis**.
15. Kobayashi, M. et al. Wettability and antifouling behavior on the surfaces of superhydrophilic polymer brushes. *Langmuir* **28**, 7212–7222 (2012).
16. Liu, M., Wang, S., Wei, Z., Song, Y. & Jiang, L. Bioinspired design of a superoleophobic and low adhesive water/solid interface. *Adv. Mater.* **21**, 665–669 (2009).
17. Kreder, M. J., Alvarenga, J., Kim, P. & Aizenberg, J. Design of anti-icing surfaces: smooth, textured or slippery? *Nat. Rev. Mater.* **1**, 1–15 (2016).
18. Amini, S. et al. Preventing mussel adhesion using lubricant-infused materials. *Science* **357**, 668–673 (2017).
19. Sunny, S. et al. Transparent antifouling material for improved operative field visibility in endoscopy. *Proc. Natl Acad. Sci. USA* **113**, 11676–11681 (2016).
20. Bocquet, L. & Lauga, E. A smooth future? *Nat. Mater.* **10**, 334–337 (2011).
21. Xu, M. et al. Superhydrophobic drag reduction for turbulent flows in open water. *Phys. Rev. Appl.* **13**, 034056 (2020).
22. Jin, M. et al. Superhydrophobic aligned polystyrene nanotube films with high adhesive force. *Adv. Mater.* **17**, 1977–1981 (2005).
23. Law, K.-Y. Water–surface interactions and definitions for hydrophilicity, hydrophobicity and superhydrophobicity. *Pure Appl. Chem.* **87**, 759–765 (2015).
24. Drelich, J. W. Contact angles: From past mistakes to new developments through liquid-solid adhesion measurements. *Adv. Colloid Interface Sci.* **267**, 1–14 (2019).
25. Drelich, J. W. et al. Contact angles: history of over 200 years of open questions. *Surf. Innov.* **8**, 3–27 (2020). **Excellent review paper on contact angles**.
26. Law, K.-Y. Contact angle hysteresis on smooth/flat and rough surfaces. interpretation, mechanism, and origin. *Acc. Mater. Res.* **3**, 1–7 (2021). **Interesting perspective on contact angles**.
27. Quéré, D. Non-sticking drops. *Rep. Prog. Phys.* **68**, 2495 (2005).
28. Roach, P., Shirtcliffe, N. J. & Newton, M. I. Progess in superhydrophobic surface development. *Soft Matter* **4**, 224–240 (2008).
29. Daniel, D., Timonen, J. V. I., Li, R., Velling, S. J. & Aizenberg, J. Oleoplaning droplets on lubricated surfaces. *Nat. Phys.* **13**, 1020–1025 (2017).
30. Decker, E. L., Frank, B., Suo, Y. & Garoff, S. Physics of contact angle measurement. *Colloids Surf. A Physicochem. Eng. Asp.* **156**, 177–189 (1999).
31. Schellenberger, F., Encinas, N., Vollmer, D. & Butt, H.-J. How water advances on superhydrophobic surfaces. *Phys. Rev. Lett.* **116**, 096101 (2016).

32. Daniel, D. et al. Origins of extreme liquid-repellency on structured, flat, and lubricated surfaces. *Phys. Rev. Lett.* **120**, 244503 (2018).

33. Daniel, D. et al. Hydration lubrication of polyzwitterionic brushes leads to nearly friction- and adhesion-free droplet motion. *Commun. Phys.* **2**, 105 (2019a). **Illustrates the ability of force-based method to measure wetting forces dynamically and to probe the physical origin of surface wetting**.

34. Semprebon, C., Sadullah, M. S., McHale, G. & Kusumaatmaja, H. Apparent contact angle of drops on liquid infused surfaces: geometric interpretation. *Soft Matter* **17**, 9553–9559 (2021).

35. Butt, H.-J. et al. Characterization of super liquid-repellent surfaces. *Curr. Opin. Colloid Interface Sci.* **19**, 343–354 (2014). **Excellent review paper that covers the theory behind vertical force measurements**.

36. Marmur, A., Volpe, C. D., Siboni, S., Amirfazli, A. & Drelich, J. W. Contact angles and wettability: towards common and accurate terminology. *Surf. Innov.* **5**, 3–8 (2017).

37. Wells, G. G. et al. Snap evaporation of droplets on smooth topographies. *Nat. Comm.* **9**, 1–7 (2018).

38. Richard, D., Clanet, C. & Quéré, D. Contact time of a bouncing drop. *Nature* **417**, 811–811 (2002).

39. Bird, J. C., Dhiman, R., Kwon, H.-M. & Varanasi, K. K. Reducing the contact time of a bouncing drop. *Nature* **503**, 385–388 (2013).

40. Volpe, C. D. & Siboni, S. The Wilhelmy method: a critical and practical review. *Surf. Innov.* **6**, 120–132 (2018). **Excellent review on Wilhelmy method**.

41. Pilat, D. W. et al. Dynamic measurement of the force required to move a liquid drop on a solid surface. *Langmuir* **28**, 16812–16820 (2012).

42. Liimatainen, V. et al. Mapping microscale wetting variations on biological and synthetic water-repellent surfaces. *Nat. Commun.* **8**, 1798 (2017). **Sub-millimetric spatial mapping of wetting properties with custom-made instrument**.

43. Hokkanen, M., Backholm, M., Vuckovac, M., Zhou, Q. & Ras, R. H. A. Force-based wetting characterization of stochastic superhydrophobic coatings at nanonewton sensitivity. *Adv. Mater.* **33**, 2105130 (2021).

44. Noy, A., Frisbie, C. D., Rozsnyai, L. F., Wrighton, M. S. & Lieber, C. M. Chemical force microscopy: exploiting chemically-modified tips to quantify adhesion, friction, and functional group distributions in molecular assemblies. *J. Am. Chem. Soc.* **117**, 7943–7951 (1995).

45. Daniel, D. et al. Mapping micrometer-scale wetting properties of superhydrophobic surfaces. *Proc. Natl Acad. Sci. USA* **116**, 25008–25012 (2019b). **Sub-millimetric spatial mapping of wetting properties with droplet probe AFM**.

46. Timonen, J. V. I., Latikka, M., Ikkala, O. & Ras, R. H. A. Free-decay and resonant methods for investigating the fundamental limit of superhydrophobicity. *Nat. Comm.* **4**, 1–9 (2013). **Novel method to measure dynamic surface wetting properties**.

47. Tadmor, R. et al. Measurement of lateral adhesion forces at the interface between a liquid drop and a substrate. *Phys. Rev. Lett.* **103**, 266101 (2009).

48. Tadmor, R. et al. Solid–liquid work of adhesion. *Langmuir* **33**, 3594–3600 (2017).

49. Gao, N. et al. How drops start sliding over solid surfaces. *Nat. Phys.* **14**, 191–196 (2018).

50. McHale, G., Gao, N., Wells, G. G., Barrio-Zhang, H. & Ledesma-Aguilar, R. Friction coefficients for droplets on solids: the liquid–solid amontons' laws. *Langmuir* **38**, 4425–4433 (2022).

51. Young, T. III. an essay on the cohesion of fluids. *Philos. Trans. R. Soc.* **95**, 65–87 (1805).

52. Huhtamäki, T., Tian, X., Korhonen, J. T. & Ras, R. H. A. Surface-wetting characterization using contact-angle measurements. *Nat. Protoc.* **13**, 1521–1538 (2018).

53. Liu, K., Vuckovac, M., Latikka, M., Huhtamäki, T. & Ras, R. H. A. Improving surface-wetting characterization. *Science* **363**, 1147–1148 (2019).

54. Vuckovac, M., Latikka, M., Liu, K., Huhtamäki, T. & Ras, R. H. A. Uncertainties in contact angle goniometry. *Soft Matter* **15**, 7089–7096 (2019).

55. Marmur, A. The lotus effect: Superhydrophobicity and metastability. *Langmuir* **20**, 3517–3519 (2004).

56. Xiu, Y., Zhu, L., Hess, D. W. & Wong, C. P. Relationship between work of adhesion and contact angle hysteresis on superhydrophobic surfaces. *J. Phys. Chem. C.* **112**, 11403–11407 (2008).

57. Meiron, T. S., Marmur, A. & Saguy, I. S. Contact angle measurement on rough surfaces. *J. Colloid Interface Sci.* **274**, 637–644 (2004).

58. Extrand, C. W. Model for contact angles and hysteresis on rough and ultraphobic surfaces. *Langmuir* **18**, 7991–7999 (2002).

59. Li, W. & Amirfazli, A. A thermodynamic approach for determining the contact angle hysteresis for superhydrophobic surfaces. *J. Colloid Interface Sci.* **292**, 195–201 (2005).

60. Kung, C. H., Sow, P. K., Zahiri, B. & Mérida, W. Assessment and interpretation of surface wettability based on sessile droplet contact angle measurement: Challenges and opportunities. *Adv. Mater. Interfaces* **6**, 1900839 (2019).

61. Tadmor, R. Open problems in wetting phenomena: Pinning retention forces. *Langmuir* **37**, 6357–6372 (2021).

62. Pierce, E., Carmona, F. J. & Amirfazli, A. Understanding of sliding and contact angle results in tilted plate experiments. *Colloids Surf. A Physicochem. Eng. Asp.* **323**, 73–82 (2008).

63. Krasovitski, B. & Marmur, A. Drops down the hill: theoretical study of limiting contact angles and the hysteresis range on a tilted plate. *Langmuir* **21**, 3881–3885 (2005).

64. Wong, W. S. Y. et al. Adaptive wetting of polydimethylsiloxane. *Langmuir* **36**, 7236–7245 (2020).

65. Joshipura, I. D. et al. Are contact angle measurements useful for oxide-coated liquid metals? *Langmuir* **37**, 10914–10923 (2021).

66. Konduru, V. Static and dynamic contact angle measurement on rough surfaces using sessile drop profile analysis with application to water management in low temperature fuel cells, (2010), Michigan Technological University (2010) https://digitalcommons.mtu.edu/etds/376.

67. Wilhelmy, L. Ueber die abhängigkeit der capillaritäts-constanten des alkohols von substanz und gestalt des benetzten festen körpers. *Ann. Phys.* **195**, 177–217 (1863).

68. Moghaddam, M. S., Claesson, P. M., Walinder, M. E. P. & Swerin, A. Wettability and liquid sorption of wood investigated by Wilhelmy plate method. *Wood Sci. Technol.* **48**, 161–176 (2014).

69. Bachmann, J., Woche, S. K., Goebel, M.-O., Kirkham, M. B., & Horton, R. Extended methodology for determining wetting properties of porous media, *Water Resour. Res.* **39** (2003).

70. Park, J. et al. Characterization of non-uniform wettability on flame-treated polypropylene-film surfaces. *J. Adhes. Sci. Technol.* **17**, 643–653 (2003).

71. Garcia, R. A., Cloutier, A. & Riedl, B. Chemical modification and wetting of medium density fibreboard panels produced from fibres treated with maleated polypropylene wax. *Wood Sci. Technol.* **40**, 402 (2005).

72. Kleingartner, J. A., Srinivasan, S., Mabry, J. M., Cohen, R. E. & McKinley, G. H. Utilizing dynamic tensiometry to quantify contact angle hysteresis and wetting state transitions on nonwetting surfaces. *Langmuir* **29**, 13396–13406 (2013).

73. Volpe, C. D., Fambri, L., Siboni, S. & Brugnara, M. Wettability of porous materials iii: Is the Wilhelmy method useful for fabrics analysis? *J. Adhes. Sci. Technol.* **24**, 149–169 (2010).

74. Ahmad, I. & Kan, C.-W. A review on development and applications of bio-inspired superhydrophobic textiles, *Materials* **9** (2016).

75. Extrand, C. W. Uncertainty in contact angle estimates from a Wilhelmy tensiometer. *J. Adhes. Sci. Technol.* **29**, 2515–2520 (2015).

76. Budziak, C. J. & Neumann, A. W. Automation of the capillary rise technique for measuring contact angles. *Colloids Surf.* **43**, 279–293 (1990).

77. Kwok, D. Y., Budziak, C. J. & Neumann, A. W. Measurements of static and low rate dynamic contact angles by means of an automated capillary rise technique. *J. Colloid Interface Sci.* **173**, 143–150 (1995).

78. Lhermerout, R., Perrin, H., Rolley, E., Andreotti, B. & Davitt, K. A moving contact line as a rheometer for nanometric interfacial layers. *Nat. Comm.* **7**, 1–6 (2016).

79. Lhermerout, R. Mouillage de surfaces désordonnées à l'échelle nanométrique, Ph.D. thesis, PSL Research University (2016).

80. Park, J., Pasaogullari, U. & Bonville, L. Wettability measurements of irregular shapes with Wilhelmy plate method. *Appl. Surf. Sci.* **427**, 273–280 (2018).

81. Backholm, M. et al. Water droplet friction and rolling dynamics on superhydrophobic surfaces. *Commun. Mater.* **1**, 64 (2020).

82. Hinduja, C. et al. Scanning drop friction force microscopy, *Langmuir* **38**, 14635–14643 (2022).

83. Shi, C. et al. Measuring forces and spatiotemporal evolution of thin water films between an air bubble and solid surfaces of different hydrophobicity. *ACS Nano* **9**, 95–104 (2015a).

84. Shi, C. et al. Long-range hydrophilic attraction between water and polyelectrolyte surfaces in oil. *Angew. Chem. Int. Ed.* **55**, 15017–15021 (2016).

85. Daniel, D. et al. Quantifying surface wetting properties using droplet probe atomic force microscopy. *ACS Appl. Mater. Interfaces* **12**, 42386–42392 (2020).

86. Suda, H. & Yamada, S. Force measurements for the movement of a water drop on a surface with a surface tension gradient. *Langmuir* **19**, 529–531 (2003).

87. Lagubeau, G., Merrer, M. L., Clanet, C. & Quéré, D. Leidenfrost on a ratchet. *Nat. Phys.* **7**, 395–398 (2011).

88. Mannetje, D. et al. Electrically tunable wetting defects characterized by a simple capillary force sensor. *Langmuir* **29**, 9944–9949 (2013).

89. M, K. R., Misra, S. & Mitra, S. K. Friction and adhesion of microparticle suspensions on repellent surfaces. *Langmuir* **36**, 13689–13697 (2020).

90. Backholm, M. & Bäumchen, O. Micropipette force sensors for in vivo force measurements on single cells and multicellular microorganisms. *Nat. Protoc.* **14**, 594–615 (2019).

91. Laroche, A. et al. Tuning static drop friction, *Droplet* **2**, e42 (2023).

92. Reyssat, M. & Quéré, D. Contact angle hysteresis generated by strong dilute defects. *J. Phys. Chem. B* **113**, 3906–3909 (2009).

93. Wang, L. & McCarthy, T. J. Covalently attached liquids: instant omniphobic surfaces with unprecedented repellency. *Angew. Chem. Int. Ed.* **55**, 244–248 (2016).

94. Extrand, C. W. & Kumagi, Y. Liquid drops on an inclined plane: the relation between contact angles, drop shape, and retentive force. *Colloid Interface Sci.* **170**, 515–521 (1995).

95. ElSherbini, A. I. & Jacobi, A. M. Retention forces and contact angles for critical liquid drops on non-horizontal surfaces. *Colloid Interface Sci.* **299**, 841–849 (2006).

96. Samuel, B., Zhao, H. & Law, K.-Y. Study of wetting and adhesion interactions between water and various polymer and superhydrophobic surfaces. *J. Phys. Chem. C.* **115**, 14852–14861 (2011).

97. Dong, Z. et al. Superoleophobic slippery lubricant-infused surfaces: Combining two extremes in the same surface. *Adv. Mater.* **30**, 1803890 (2018).

98. Dong, Z. et al. 3D Printing of Superhydrophobic Objects with Bulk Nanostructure. *Adv. Mater.* **33**, 2106068 (2021).

99. Shyam, S., Misra, S. & Mitra, S. K. A universal capillary-deflection based adhesion measurement technique. *J. Colloid Interface Sci.* **630**, 322–333 (2023).

100. Yao, X., Gao, J., Song, Y. & Jiang, L. Superoleophobic surfaces with controllable oil adhesion and their application in oil transportation. *Adv. Func. Mater.* **21**, 4270–4276 (2011).

101. Shi, C. et al. Interaction between air bubbles and superhydrophobic surfaces in aqueous solutions. *Langmuir* **31**, 7317–7327 (2015).

102. Vuckovac, M., Backholm, M., Timonen, J. V. I. & Ras, R. H. A. Viscosity-enhanced droplet motion in sealed superhydrophobic capillaries. *Sci. Adv.* **6**, eaba5197 (2020).

103. Adera, S. et al. Depletion of lubricant from nanostructured oil-infused surfaces by pendant condensate droplets. *ACS Nano* **14**, 8024–8035 (2020).

104. Brutin, D. & Starov, V. Recent advances in droplet wetting and evaporation. *Chem. Soc. Rev.* **47**, 558–585 (2018).

105. Kuang, M., Wang, L. & Song, Y. Controllable printing droplets for high-resolution patterns. *Adv. Mater.* **26**, 6950–6958 (2014).

106. Biance, A.-L., Chevy, F., Clanet, C., Lagubeau, G. & Quéré, D. On the elasticity of an inertial liquid shock. *J. Fluid Mech.* **554**, 47–66 (2006).

107. Miljkovic, N. & Wang, E. N. Condensation heat transfer on superhydrophobic surfaces. *MRS Bull.* **38**, 397–406 (2013).

108. Binnig, G., Quate, C. F. & Gerber, C. H. Atomic force microscope. *Phys. Rev. Lett.* **56**, 930–933 (1986).

109. Noy, A., Vezenov, D. V. & Lieber, C. M. Chemical force microscopy. *Annu. Rev. Mater. Sci.* **27**, 381–421 (1997).

110. Woolley, A. T., Cheung, C. L., Hafner, J. H. & Lieber, C. M. Structural biology with carbon nanotube afm probes. *Chem. Bio.* **7**, R193–R204 (2000).

111. Hassenkam, T., Skovbjerg, L. L. & Stipp, S. L. S. Probing the intrinsically oil-wet surfaces of pores in north sea chalk at subpore resolution. *Proc. Natl Acad. Sci. USA* **106**, 6071–6076 (2009).

112. Ducker, W. A., Senden, T. J. & Pashley, R. M. Direct measurement of colloidal forces using an atomic force microscope. *Nature* **353**, 239–241 (1991).

113. Israelachvili, J. N. *Intermolecular and surface forces.* Chap. 14 (Academic press, 2011).

114. Manor, O. et al. Hydrodynamic boundary conditions and dynamic forces between bubbles and surfaces. *Phys. Rev. Lett.* **101**, 024501 (2008).

115. Daniel, D., Goh, S. S., Truong, T. N. B., Koh, X. Q. & Tomczak, N. Origin of underwater oil-repellence in polyelectrolyte brush surfaces. *Adv. Mater. Interfaces* **8**, 2001203 (2021).

116. Méndez-Vilas, A., Jódar-Reyes, A. B. & González-Martín, M. L. Ultrasmall liquid droplets on solid surfaces: production, imaging, and relevance for current wetting research. *small* **5**, 1366–1390 (2009).

117. Delmas, M., Monthioux, M. & Ondarçuhu, T. Contact angle hysteresis at the nanometer scale. *Phys. Rev. Lett.* **106**, 136102 (2011).

118. Al-Azawi, A., Latikka, M., Jokinen, V., Franssila, S. & Ras, R. H. A. Friction and wetting transitions of magnetic droplets on micropillared superhydrophobic surfaces. *Small* **13**, 1700860 (2017).

119. Rosensweig, R. E. *Ferrohydrodynamics* (Courier Corporation, 2013).

120. Joseph, A. & Mathew, S. Ferrofluids: synthetic strategies, stabilization, physicochemical features, characterization, and applications. *ChemPlusChem* **79**, 1382 (2014).

121. Torres-Díaz, I. & Rinaldi, C. Recent progress in ferrofluids research: novel applications of magnetically controllable and tunable fluids. *Soft Matter* **10**, 8584–8602 (2014).

122. Backholm, M. et al. Oscillating ferrofluid droplet microrheology of liquid-immersed sessile droplets. *Langmuir* **33**, 6300–6306 (2017).

123. Latikka, M., Backholm, M., Timonen, J. V. I. & Ras, R. H. A. Wetting of ferrofluids: Phenomena and control. *Curr. Opin. Colloid Interface Sci.* **36**, 118–129 (2018).

124. Sun, Q. et al. Surface charge printing for programmed droplet transport. *Nat. Mater.* **18**, 936–941 (2019).

125. Lin, S., Xu, L., Wang, A. C. & Wang, Z. L. Quantifying electron-transfer in liquid-solid contact electrification and the formation of electric double-layer. *Nat. Comm.* **11**, 399 (2020).

126. Rayleigh, L. & Pockels, A. Surface tension. *Nature* **43**, 437 (1891).

127. Collins, G. E. A surface tension method for measuring the perimeters of fibres and the contact angles of liquids against fibres. *J. Text. Inst. Trans.* **38**, T73–T77 (1947).

128. Furmidge, C. G. L. Studies at phase interfaces. i. the sliding of liquid drops on solid surfaces and a theory for spray retention. *J. Colloid Sci.* **17**, 309–324 (1962).

Acknowledgements

Author contributions

D.D., N.T., and R.H.A.R. initiated the project. D.D., M.V., and M.B. wrote the bulk of this review. All authors (including M.L., R.K., X.Q.K., and J.V.I.T.) contributed to the writing and approved the final manuscript.

Competing interests

N.T. is an Editorial Board Member for Communications Physics, but was not involved in the editorial review of, or the decision to publish this article. The other authors declare no other competing interests.

Additional information

Supplementary information The online version contains supplementary material available at https://doi.org/10.1038/s42005-023-01268-z.

Correspondence and requests for materials should be addressed to Dan Daniel, Nikodem Tomczak or Robin H. A. Ras.

Peer review information *Communications Physics* thanks Zuankai Wang and the other, anonymous, reviewer(s) for their contribution to the peer review of this work. A peer review file is available.

Reprints and permission information is available at http://www.nature.com/reprints

Publisher's note Springer Nature remains neutral with regard to jurisdictional claims in published maps and institutional affiliations.